



## **Final Draft of the original manuscript**

Hasija, V.; Kumar, A.; Sudhaik, A.; Raizada, P.; Singh, P.; Van Le, Q.;  
Le, T.T.; Nguyen, V.-H.:

**Step-scheme heterojunction photocatalysts for solar energy,  
water splitting, CO<sub>2</sub> conversion, and bacterial inactivation: a  
review.**

In: Environmental Chemistry Letters. Vol. 19 (2021) 4, 2941 – 2966.

First published online by Springer: 02.04.2021

<https://dx.doi.org/10.1007/s10311-021-01231-w>

# Step-scheme heterojunction photocatalysts for solar energy, water splitting, CO<sub>2</sub> conversion, and bacterial inactivation: a review

Vasudha Hasija<sup>1</sup> · Abhinandan Kumar<sup>1</sup> · Anita Sudhaik<sup>1</sup> · Pankaj Raizada<sup>1</sup> · Pardeep Singh<sup>1</sup> · Quyet Van Le<sup>2</sup> · Thi Thu Le<sup>3</sup> · Van-Huy Nguyen<sup>4,5</sup>

Solar radiation is a sustainable, unlimited source of energy for electricity and chemical reactions, yet the conversion efficiency of actual processes is limited and controlled by photocarriers migration and separation. Enhancing the conversion efficiency would require to suppress the recombination of photogenerated electron-hole pairs and improve the low redox potentials. This can be done during the growth of step-scheme (S-scheme) heterojunctions. Here we review the charge transfer of S-scheme heterojunctions involving a reduction and oxidation photocatalyst in staggered band arrangement with Fermi level differences. We present factors determining the validation of the S-scheme mechanism with respective characterization techniques, including in situ and ex situ experiments, and theoretical studies. We show mechanistic drawbacks of traditional photocatalytic systems to highlight the advantages of S-scheme photocatalysts. We describe co-catalyst loading, bandgap tuning, and interfacial optimization that ultimately achieve highly efficient photocatalysis. Last, application for water splitting, CO<sub>2</sub> conversion, pollutant degradation, bacterial inactivation and others is discussed.

## Introduction

Photocatalysis has been envisioned as an innovative advanced oxidation process to sustain inexhaustible solar energy. The inspiration for photocatalysis was the natural photosynthesis process to convert and store photonic energy into usable chemical energy (Xu, C. et al. 2019). Photocatalysis possesses vital advantages over traditional catalytic processes involving temperature, pressure independence, elimination of tedious steps, and unrestricted employment of only metal-based catalysts (Gao et al. 2017). Since the development of TiO<sub>2</sub> electrodes based first photoelectrochemical cell by Fujishima and Honda in 1972 (Fujishima and Honda, 1972), semiconductor photocatalysis has emerged into multidisciplinary research fields (Kanakaraju et al. 2014; Liras et al. 2019; Mecha and Chollom, 2020; Mousset and Dionysiou, 2020; Saravanan et al. 2021). The extensively exploited photocatalytic applications are directed for organic synthesis (Nguyen et al. 2012, 2015; Nguyen, V.-H. et al. 2020b), water splitting into H<sub>2</sub>/O<sub>2</sub> (Huang et al. 2020; Kalyanasundaram, 2013; Li et al. 2018; Soni et al. 2021), pollutant mineralization (Nguyen, T.D. et al. 2020; Nguyen, V.-H.

---

Pankaj Raizada  
pankajchem1@gmail.com

Pardeep Singh  
pardeepchem@gmail.com

Van-Huy Nguyen  
nguyenvanhuy@tdtu.edu.vn

<sup>1</sup> School of Advanced Chemical Sciences, Shoolini University, Solan, HP, India 173229

<sup>2</sup> Institute of Research and Development, Duy Tan University, Da Nang 550000, Vietnam

<sup>3</sup> Institute of Hydrogen Technology, Materials Design, Helmholtz-Zentrum Geesthacht, Max-Planck Str. 1, 21502 Geesthacht, Germany

<sup>4</sup> Department for Management of Science and Technology Development, Ton Duc Thang University, Ho Chi Minh City, Vietnam

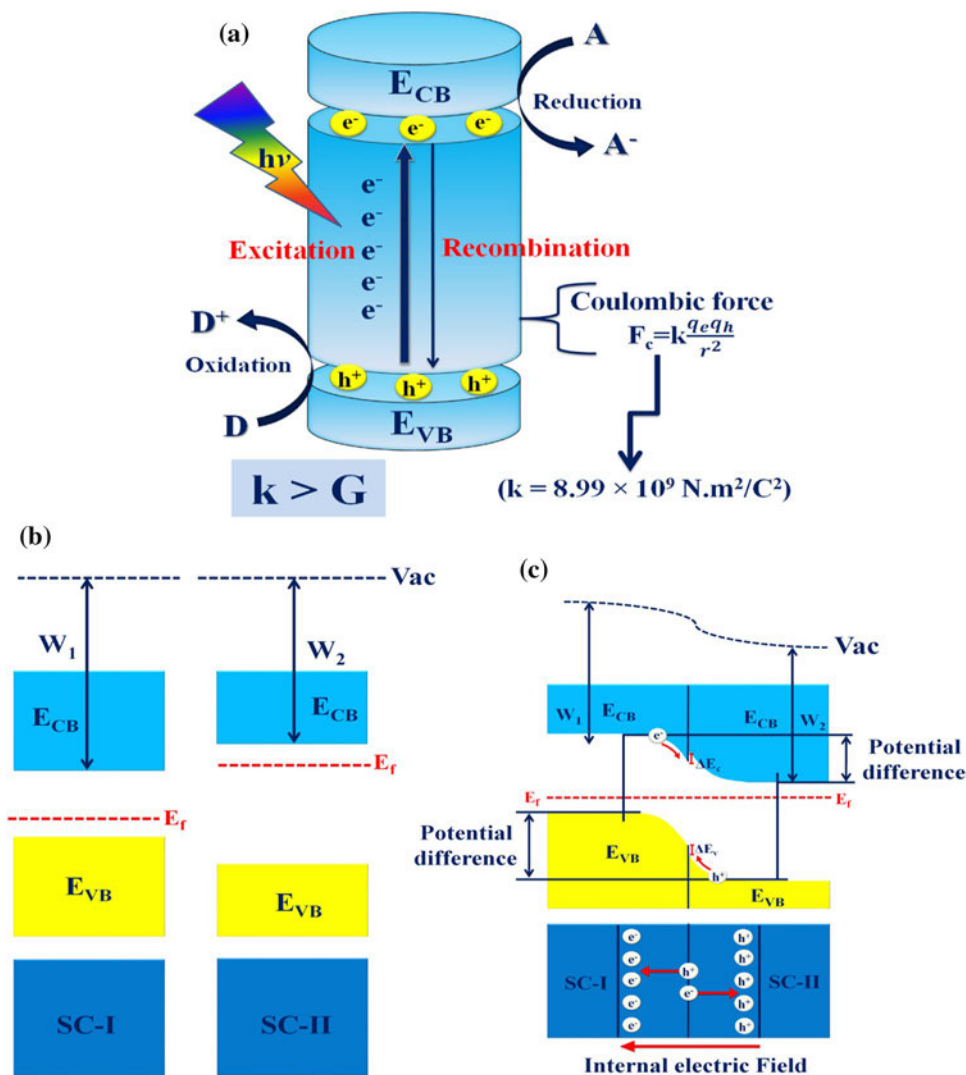
<sup>5</sup> Faculty of Applied Sciences, Ton Duc Thang University, Ho Chi Minh City, Vietnam

et al. 2020c; Nguyen, V.-H. et al. 2020d; Sharma et al. 2021; Wu et al. 2013; Yu et al. 2017; Zhu and Zhou, 2019), and CO<sub>2</sub> reduction (Chen et al. 2016; Cheng et al. 2015; Kumar et al. 2021b; Nguyen, T.P. et al. 2020; Nguyen, V.-H. et al. 2020a; Nguyen and Wu, 2018). Concisely, photocatalysis is a process in which photocatalyst absorbs photons to generate energetic holes and electrons capable of initiating oxidation and reduction reactions, respectively (Fox and Dulay, 1993).

The following complementary and indispensable steps comprise of a typical photocatalysis process (Yang and Wang, 2018), i.e.; (i) solar illumination of photocatalyst for the generation of photoexcited electron–hole pairs, (ii) charge carrier separation followed by (iii) sequential charge transfer on respective catalytic sites/surface for redox reactions as displayed (Fig. 1a). The reduction and oxidation potential of photoexcited electrons and holes depend on the conduction band minimum and valence band maximum positions, respectively. Upon irradiation of solar photons, electrons are promoted from

the valence band to conduction band, when  $h\nu > E_g$  where  $E_g$  is bandgap energy. The timescale for recombination of electron–hole pairs under the strong Coulombic forces of attraction occurs in less than  $10^{-9}$  femtoseconds (Low et al. 2017b). It is analogous to the falling of an object onto the ground under the gravitational force, where the coulombic constants ( $8.99 \times 10^9 \text{ Nm}^2/\text{C}^2$ ) are much larger than the gravitational constant i.e.,  $6.67 \times 10^{-11} \text{ Nm}^2/\text{C}^2$  (Xu et al. 2018). The reverse recombination of charge carriers impairs the functioning of photocatalytic reactions. Likewise, the accumulation of charge carriers on the photocatalytic surface might lead to unwanted semiconductor instability due to the presence of highly reductive electrons and oxidative holes. The driving force for the generation of reactive oxidative species depends upon the redox potentials of the conduction band and valence band edges for which a shallow valence band and high conduction band position is suitable (Zhu and Wang, 2017).

**Fig. 1** **a** Basic photocatalysis mechanism showing excitation of charge carriers under the illumination of light and subsequent recombination facilitated by Coulombic force; the symbols A and D represent acceptor and donor species, respectively, while  $k$  is the Coulombic force constant and  $G$  is gravitational constant, and **b** band diagrams representing the formation of a surface junction between semiconductor I (SC I) and semiconductor II (SC II) (the symbols  $W_1$ ,  $W_2$ ,  $E_{CB}$ ,  $E_{VB}$ ,  $E_f$ , and Vac depict work function of SC I, work function of SC II, conduction band energy, valence band energy, Fermi energy and vacuum level, respectively). Adapted with permission (Bai et al. 2015). Copyright 2015, Royal Society of Chemistry



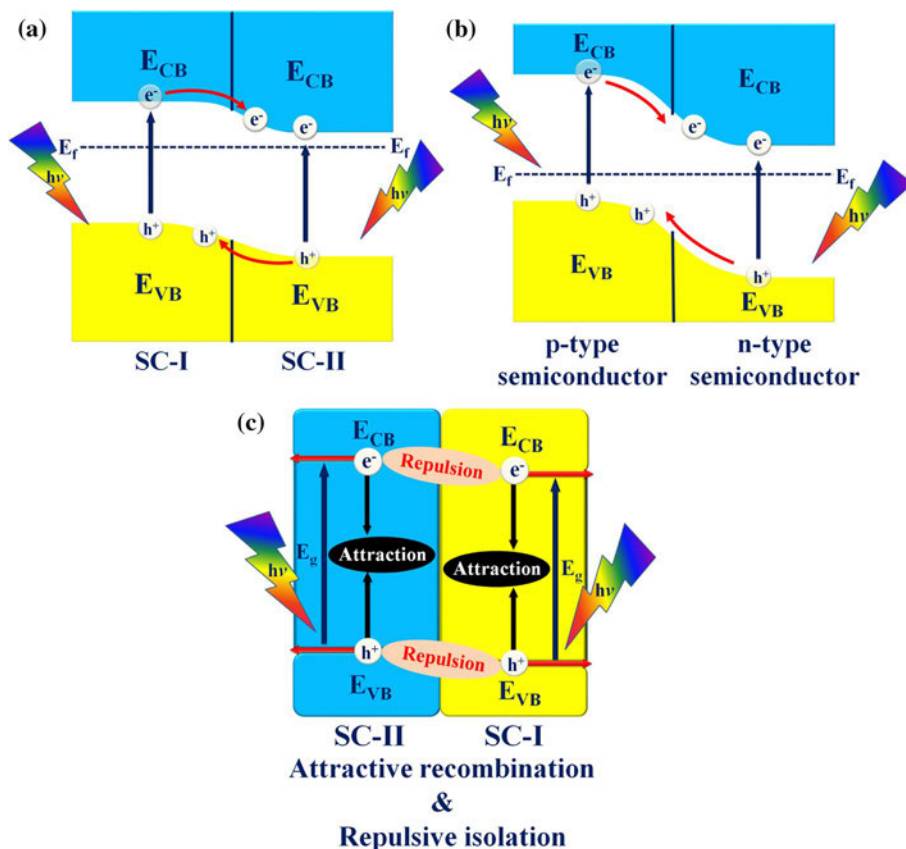
It is also imperative to achieve (i) broad sunlight absorption and (ii) the strong redox ability of a semiconductor. Since both have opposing pathways, broad light absorption is achieved via narrowing  $E_g$  of semiconductor, whereas strong redox ability is certain of wide  $E_g$  with a highly negative conduction band and positive valence band (Bagheri et al. 2017). As a result, the criteria to achieve broad light absorption and utmost redox ability are contrary. Therefore, the development of heterojunction formed by direct contact of two semiconductors is an effective architecture to mitigate the obstacles suffered by bare semiconductors (Zhong et al. 2020). The suitable band edge positions of the coupled semiconductors are beneficial for prolonged charge carriers lifetime, broadened solar light absorption, and enhanced charge carrier separation (Banerjee et al. 2014).

Considering the charge transfer mechanism in semiconductor–semiconductor heterojunction (Fig. 1b), the potential difference between two semiconductors results in charge redistribution and alignment of Fermi level ( $E_f$ ) followed by two outcomes, i.e., (i) accumulation of electrons on the semiconductor surface causing upward band bending in semiconductor II, and (ii) excessive holes on the surface, which leads to downward band bending in semiconductor I. The direction of band bending depends on the valence band and conduction band of both semiconductors (Fig. 1c). The upward band bend offers higher oxidation ability as it

attracts holes, whereas the downward band bend leads to a reduction reaction directing electrons on the surface (Bai et al. 2015). The internal electric field generated due to the formation of a space charge region facilitates charge carrier separation; still, there is a probability of recombination (Dai et al. 2020). The photoexcited charge carriers in constructed heterojunctions should overcome the built-in-internal electric field and potential differences to impede the coulombic forces of attraction between electrons and holes.

Among variant heterojunctions, the most appropriate arrangement of two semiconductors is in staggered type-II arrangement following the electron transference route from higher to lower conduction band and reverse pathway for photogenerated holes (Zheng et al. 2020). As presented in (Fig. 2a), the semiconductor I with higher  $E_f$  and lower work function ( $\phi$ ) losses electrons and bends downwards, i.e., from semiconductor I to semiconductor II. In contrast, the simultaneous migration of holes occurs from semiconductor II to semiconductor I with upward bending. The resultant band bending of semiconductor I band edges promotes accumulation of electrons onto semiconductor II for reduction reaction, whereas upward band bend leads to excessive holes on semiconductor I for the oxidation reaction. It is much evident and noteworthy that maximum electron–hole pairs separation is obtained in junctions with the difference in  $\phi$  of both semiconductors. Indeed, type-II heterojunction between

**Fig. 2** Band structure diagrams illustrating the charge migration routes in: **a** Type-II heterojunction and **b** p-n heterojunction; the symbols SC I, SC II,  $E_{VB}$ ,  $E_{CB}$ ,  $E_g$ , and  $E_f$  represent semiconductor I, semiconductor II, valence band energy, conduction band energy, bandgap energy and Fermi energy, respectively. Adapted with permission (Bai et al. 2015). Copyright 2015, Royal Society of Chemistry. **c** Schematics illustrating the major drawbacks such as recombination (between oppositely charged species) and repulsion (between similarly charged species) induced in conventional type-II heterojunction system



p-type and n-type semiconductors is beneficial over p-p and n-n type junctions due to the large difference in  $\phi$  and redox potentials. This is explained by (Fig. 2b) charge transfer in p-n heterojunction which follows electrons transference from p-type semiconductor towards higher  $E_f$  n-type semiconductor, and holes migrate to lower  $E_f$  p-type semiconductor. It is worth clarifying that the potential difference between the two semiconductors determines the charge migration route, and the internal electric field leads to charge separation (Bai et al. 2015).

Undoubtedly, type-II heterojunction charge transfer routes have ignited the plethora of photocatalysis, but it has certain ambiguities on closer examination. The type-II photocatalytic mechanism suppresses electron-hole pairs recombination but at the expense of conduction band and valence band redox potential (Fig. 2c) (Xu et al. 2020). Firstly, the thermodynamic criterion of effective charge separation in type-II leads to excessive accumulation of electrons in the conduction band of semiconductor II and holes in the valence band of the semiconductor, reducing the reduction and oxidation potentials. Secondly, the dynamic parameter of electrostatic repulsive forces between like charges, i.e., electrons-electrons and holes-holes, has been ignored. Thirdly, the lifetime of charge carriers concerning the kinetics of reverse recombination reactions and desired reactive oxidative species generation has remained unresolved (Low et al. 2017a). Thereby, the type-II charge transfer mechanism is vulnerable and tends to weaken the overall redox potential of heterojunction.

Lately, S-scheme heterojunctions with a similar configuration to the type-II system were established by Yu et al. to surmount type-II limitations (Fu et al. 2019). They claimed that the S-scheme heterojunctions could induce maximum electron-hole pairs separation and remarkably retain their redox ability under the internal electric field that develops due to different Fermi levels of photocatalysts. Afterwards, a large number of researches on S-scheme heterojunctions have sprung up in various fields of photocatalysis.

## Background of S-scheme photocatalysts

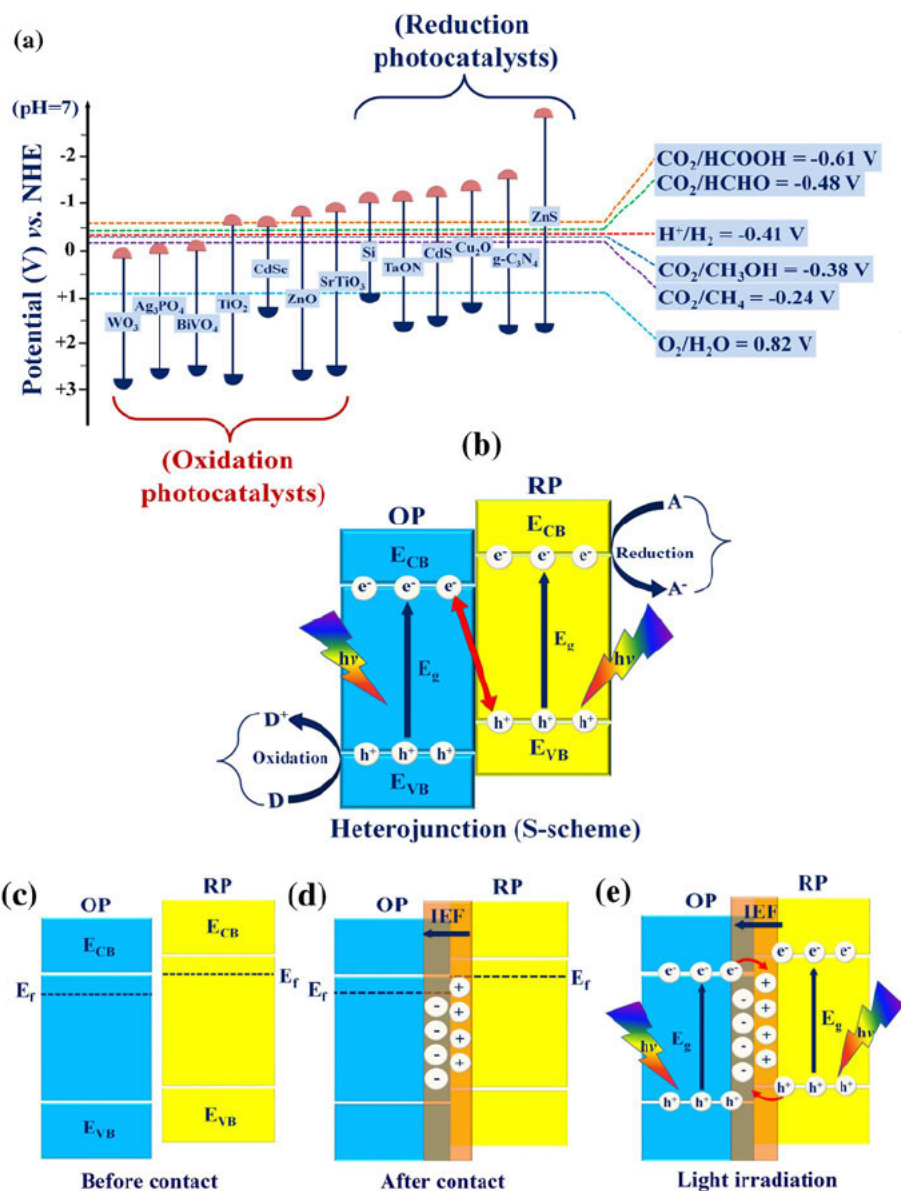
The formation of S-scheme heterojunction is solely dependent on the coupling of a reduction photocatalyst and oxidation photocatalyst differentiated based on band structures, as shown in (Fig. 3a) (Xu et al. 2020). The combination of reduction photocatalyst and oxidation photocatalyst can provide synergistic dual functionality, where the photoexcited electrons of reduction photocatalyst are utilized for solar fuel production, whereas photoexcited holes of oxidation photocatalyst are potential for effective photodegradation reactions (Chen, J. et al. 2020). The S-scheme heterojunction configuration is similar to type-II staggered configuration,

with oxidation photocatalyst and reduction photocatalyst following the distinct charge carrier transfer pathway (Cerrato and Paganini, 2020). The key advantage of S-scheme heterojunction (Fig. 3b) is a reservation of effective photogenerated electrons and holes in the conduction band of reduction photocatalyst and valence band of oxidation photocatalyst, respectively. Also, simultaneous recombination of fruitless photogenerated electrons of oxidation photocatalyst and holes reduction photocatalyst in the interfacial built-in-internal electric field region induces a strong redox potential (Zou et al. 2020). S-scheme heterojunction follows the “step-like” migration of charge carriers macroscopically and “N-shaped” from a microscopic viewpoint (Xie et al. 2020). A sequential charge-migration route is followed in an S-scheme heterojunction as explained:

- Figure 3c depicts the exemplary energy band diagrams of reduction photocatalyst and oxidation photocatalyst before contact, where reduction photocatalyst possesses higher conduction band and valence band positions. In contrast, oxidation photocatalyst has a lower conduction band and valence band edges (Xu et al. 2020). Usually, the oxidation photocatalyst has a lower Fermi level and higher  $\phi$ ; contrarily, the reduction photocatalyst has a higher Fermi level and lower  $\phi$ . The  $\phi$  difference between the two photocatalysts governs the transference of charge carriers.
- When these two photocatalysts are in close contact, as shown in (Fig. 3d), the electrons tend to flow from lower to higher  $\phi$ , i.e., from the conduction band of reduction photocatalyst to conduction band of oxidation photocatalyst. The electron transfer will continue until the Fermi levels of reduction photocatalyst and oxidation photocatalyst is in equilibrium, forming the spatial charge region (Xu et al. 2020). The diffusion of electrons from reduction photocatalyst to oxidation photocatalyst leads to the generation of depletion layer characterized by excess positive charge near the interface of reduction photocatalyst. While nearby the surface of the oxidation photocatalyst, there is an accumulation of electrons forming an accumulation layer (Bai et al. 2015).
- The generated internal electric field directed from reduction photocatalyst to oxidation photocatalyst in the spatial charge region causes two major consequences: Firstly, there is a reverse transference of electrons from the conduction band of oxidation photocatalyst towards reduction photocatalyst. Secondly, both the closely situated photocatalysts experience shifting of energy band edges, causing band bending (Fig. 3e) (Xu et al. 2020). The energy band of the oxidation photocatalyst bends downwards towards the interface while the reduction photocatalyst edges bend upwards. The direction of band bends urges the interfacial recombination of photogenerated



**Fig. 3** **a** Band edge positioning of some oxidation and reduction type photocatalysts concerning the redox potential required for various photocatalytic reactions (adapted with permission (Xu et al. 2020), Copyright 2020, CelPress). **b** Mechanistic insight into the S-scheme charge transfer mechanism showing recombination of conduction band electrons present in oxidation photocatalyst (OP) with the valence band holes of reduction photocatalyst at the interface followed by subsequent photoredox reactions resulting in the reduction and oxidation of acceptor (A) and donor (D), respectively. Band diagrams of oxidation photocatalyst (OP) and reduction photocatalyst **c** before contact, **d** after contact and **e** charge migration process under the illumination of light. (The symbols IEF, EVB, ECB, and  $E_g$  represent an internal electric field, valence band energy, conduction band energy, and bandgap energy, respectively)



electrons in the conduction band of oxidation photocatalyst and valence band holes of reduction photocatalyst due to the columbic attraction between the opposite charges (Tao et al. 2021).

- Subsequently, the powerful redox potential of deeper valence band holes and higher conduction band electrons is preserved and contributes to the oxidation and reduction reactions, respectively. The S-scheme mechanism simultaneously comprehends high solar energy conversion efficiency, charge separation, and surface redox reaction (Xu et al. 2019).

Hence, the formation of S-scheme heterojunction amidst two semiconductors is a constructive tactic in

promoting the segregation of electron–hole pairs by an S-shaped charge transportation route with enhanced redox capability. The S-scheme mechanism is driven by the difference in  $\phi$  of oxidation photocatalyst and reduction photocatalyst, which is responsible for generating an internal electric field. Further, the internal electric field determines electron–hole pairs separation in the spatial charge region. The presence of band bending and a potential difference is associated with the specific reductive and oxidative photocatalytic reactions. The superiority of the S-scheme is the elimination of the useless electrons and holes with simultaneous preservation of reduction photocatalyst electrons and holes of oxidation photocatalyst.

## S-scheme mechanism

The arrangement of the conduction band and valence band in the S-scheme photocatalyst is similar to that of type-II heterojunctions. Hence, it is imperious to experimentally identify the charge migration route in S-scheme heterojunctions for its distinction from type-II systems. The characterization techniques involved are in/ex situ experiments and theoretical simulation studies (Zhang et al. 2019), which justifies the molecular and atomic levels of S-scheme heterojunction photocatalysts. The following are the proposed factors and respective characterization tools to elucidate the S-scheme mechanism:

### Variation in electron density

It is well observed in the S-scheme charge transfer mechanism that oxidation photocatalyst and reduction photocatalyst undergo a decrease or increase in electron density before and after contact, i.e., without light irradiation and in light irradiation. The change in electron density is comprehended by ex and in situ irradiated X-ray photoelectron spectroscopy analysis. For instance, X-ray photoelectron spectroscopy characterization of layered black phosphorus/BiOBr heterojunction confirmed the S-scheme charge transfer route. Figure 4 a, c) demonstrates the high-resolution spectra of P 2p in bare black phosphorus and 10% black phosphorus/BiOBr composite, where the characteristic peak of P 2p<sub>3/2</sub> and 2p<sub>1/2</sub> displayed a shift of 0.15 eV towards lower energy in the 10% black phosphorus/BiOBr composite relative to bare black phosphorus. The negative shift of binding energies from 129.9 eV to 129.75 eV is indicative of an increase in electron density on the interface of BiOBr. The existence of 133.4 eV peak of O-P=O functional group (Fig. 4c) confirmed the formation of P-O-Bi strong chemical bonds between the black phosphorus and BiOBr heterojunction photocatalysts. Similarly, P-O-Bi peak was present in Bi (4f) (Fig. 4d) of 10% black phosphorus/BiOBr, whereas no P-O-Bi peak was found in bare BiOBr (Fig. 4b).

The X-ray photoelectron spectroscopy results were evident in interfacial interaction between black phosphorus and BiOBr (Fig. 4e), and the disturbance in electron density generates accumulation and depletion layer at BiOBr and BP interface, respectively. The increased electron density on BiOBr was attributed to the induced internal electric field and e<sup>-</sup> transference from lower  $\phi$ , i.e., 5.65 eV black phosphorus to 6.25 eV (BiOBr) until the Fermi level equilibrates. The charge migration route between black phosphorus and BiOBr was following the S-scheme mechanism (Fig. 4f) where the conduction band

electrons of BiOBr recombined with valence band holes of black phosphorus in the interface region (Li et al. 2020). The sufficiently high redox potential of BP with -1.02 eV and oxidation potential of BiOBr (2.53 eV) caused the generation of O<sub>2</sub><sup>-</sup> and ·OH reactive species for the dual application of O<sub>2</sub> evolution and tetracycline (TC) antibiotic photodegradation; furthermore, the X-ray photoelectron spectroscopy analysis of Bi<sub>2</sub>O<sub>3</sub>/TiO<sub>2</sub> nanofibers confirmed the S-scheme charge carrier process under UV-Vis irradiations. The Bi 4f high-resolution spectrum of bare Bi<sub>2</sub>O<sub>3</sub> displayed blueshift in Bi<sub>2</sub>O<sub>3</sub>/TiO<sub>2</sub> composite from 164.0 to 164.6 eV and 158.7 to 159.3 eV for Bi 4f<sub>5/2</sub> and 4f<sub>7/2</sub> orbitals, respectively. This was indicative of decreased electron density on Bi<sub>2</sub>O<sub>3</sub> due to electron transference from Bi<sub>2</sub>O<sub>3</sub> to TiO<sub>2</sub> under the influence of the internal electric field (Rongan et al. 2020). The changes in binding energies unequivocally confirm the charge separation and migration process.

### Recombination of lower redox potential electron-hole pairs

Factually, rapid charge carrier recombination is detrimental to all photocatalytic applications. Captivatingly, S-scheme unique charge transfer mechanism favors the high charge separation efficiency of strong redox power charge carriers, while the useless photogenerated electrons and holes with weak redox ability recombine. The electron paramagnetic resonance signals indicate the produced reactive oxidative species via higher redox potential photogenerated electrons and holes, thereby supporting the S-scheme preservation strategy.

This hypothesis is proven in CdZnS/g-C<sub>3</sub>N<sub>4</sub> heterojunction electron paramagnetic resonance results (Fig. 5a) where 5,5- dimethyl-pyrroline- N oxide-O<sub>2</sub><sup>-</sup> the signal was observed for g-C<sub>3</sub>N<sub>4</sub> revealing a higher reduction ability to reduce O<sub>2</sub> to O<sub>2</sub><sup>-</sup> for rhodamine B dye degradation. Contrarily the 5,5- dimethyl-pyrroline- N oxide ·OH (Fig. 5b) is negligible as both the CdZnS and g-C<sub>3</sub>N<sub>4</sub> lacks the minimum potential for release of ·OH. This suggests that photogenerated electrons and holes remain static in the conduction band of g-C<sub>3</sub>N<sub>4</sub> and valence band of CdZnS, respectively. This assures the S-scheme charge carrier pathway over the type-II heterojunction mechanism shown in (Fig. 5c) where the sequential processes jointly discard the type-II charge transfer route. Noticeably, the lower  $\phi$  of g-C<sub>3</sub>N<sub>4</sub> (4.3 eV) than 6.7 eV of CdZnS caused e<sup>-</sup> transference from g-C<sub>3</sub>N<sub>4</sub> to CdZnS until their Fermi levels are aligned, with the formation of the electron depletion layer in g-C<sub>3</sub>N<sub>4</sub> and accumulation layer at the interface of CdZnS. Subsequently, the upward band bending in g-C<sub>3</sub>N<sub>4</sub> and downward bending in CdZnS reduce the oxidation abilities. The generated internal electric field in the space charge region, oriented from

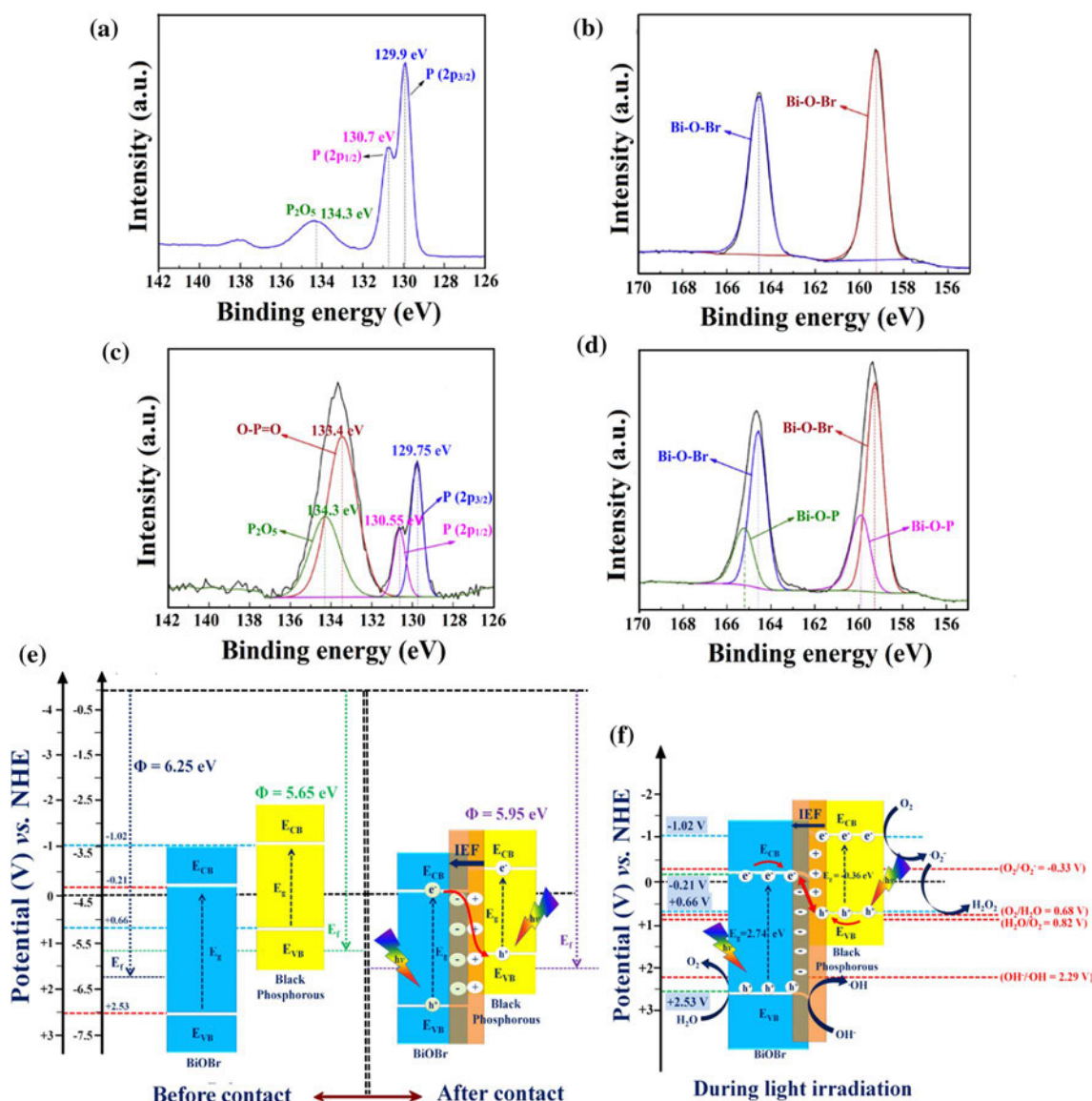


**Fig. 4** High-resolution X-ray photoelectron spectroscopy (XPS) survey spectra of **a** P 2p of pure black phosphorous, **b** Bi 4f of pristine BiOBr, **c** P 2p and **d** Bi 4f of optimized black phosphorous nanosheets coupled with BiOBr nanosheets through solvothermal treatment (Sol-10BP/BiOBr nanocomposite). Reproduced with permission (Li et al. 2020). Copyright 2020, Elsevier. Schematic illustration of **e** band diagrams of black phosphorous nanosheets and

BiOBr nanosheets before contact and **f** subsequent S-scheme charge transfer route under light irradiation,  $\Phi$  and  $E_f$  represent the work function and Fermi energy level of black phosphorous and BiOBr, which induced the formation of the internal electric field at the interface resulted into facile migration and isolation of photo-carriers. Adapted with permission (Li et al. 2020). Copyright 2020, Elsevier

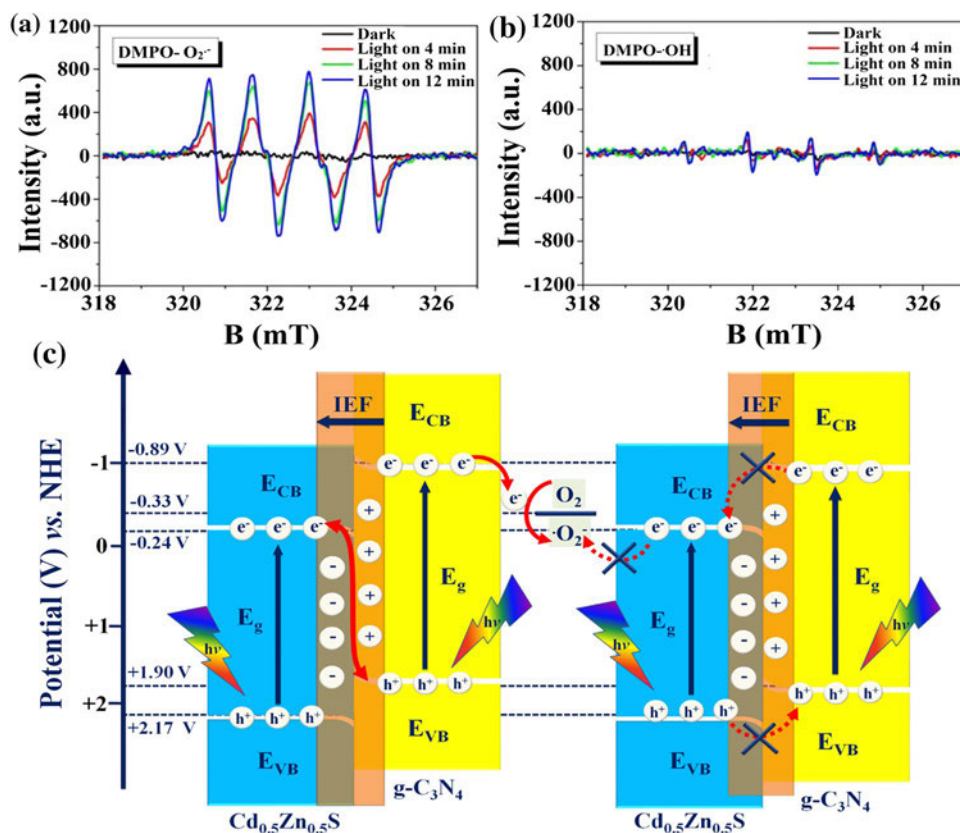
g- $C_3N_4$  to CdZnS, prevents migration of electrons and holes via the type-II route and induces recombination of useless CdZnS electrons and holes of g- $C_3N_4$  (Qin, D. et al. 2020a).

The identification and confirmation of major reactive species were observed by the electron paramagnetic resonance results in spinel ferrite-based  $SnFe_2O_4$ - $ZnFe_2O_4$  composite. The electron paramagnetic resonance spectra revealed 5,5-dimethyl-pyrroline-N oxide- $O_2^{\cdot-}$  and  $\cdot OH$  peak signals under visible light irradiations suggestive of  $O_2^{\cdot-}$  and  $\cdot OH$  as the significant reactive oxidative species. However, the

release of  $\cdot OH$  was not possible due to lower valence band potentials of  $SnFe_2O_4$  and  $ZnFe_2O_4$ , i.e., 1.54 and 1.55 V. Hence, the possible release of  $\cdot OH$  was mainly by the reaction of  $O_2^{\cdot-}$  with  $H_2O$  molecules, which were well in agreement with the -0.33 V conduction band potential of  $SnFe_2O_4$  with simultaneous recombination of photogenerated conduction band electrons of  $ZnFe_2O_4$  with the holes of  $SnFe_2O_4$  under the driving force of internal electric field (Wang, J. et al. 2020). Thus, electron paramagnetic resonance spectra corroborate the S-scheme mechanism route by confirming



**Fig. 5** Electron spin resonance spectra of  $\text{Cd}_{0.5}\text{Zn}_{0.5}\text{S}/\text{g-C}_3\text{N}_4$  sample showing spin-trapping experiment results by using a 5,5-dimethyl-1-pyrroline-N-oxide agent for **a**  $\text{O}_2^{\cdot-}$  radicals and **b**  $\cdot\text{OH}$  radicals. Reprinted with permission (Qin, D. et al. 2020a). Copyright 2020, Elsevier. **c** Diagrammatic representation of the feasible S-scheme charge migration over the conventional type-II route in  $\text{Cd}_{0.5}\text{Zn}_{0.5}\text{S}/\text{g-C}_3\text{N}_4$  heterojunction system. The formation of the internal electric field at the interface of  $\text{Cd}_{0.5}\text{Zn}_{0.5}\text{S}$  and  $\text{g-C}_3\text{N}_4$  due to the redistribution of charge carriers facilitated the migration of photocarriers through S-scheme mode. Adapted with permission (Qin, D. et al. 2020a). Copyright 2020, Elsevier



released reactive oxidative species and lower redox potential electrons and holes recombination.

### Appropriate interfacial contact

In the S-scheme heterojunction, effective charge-carrier migration/separation is possible only when there is sufficient interfacial contact between oxidation photocatalyst and reduction photocatalyst. Atomic force microscopy examines the intimacy between heterojunction photocatalysts and the increase in surface oxidation potential of oxidation photocatalyst due to electron transfer from oxidation photocatalyst to reduction photocatalyst.

For example, the 2D/2D surface-surface heterojunction between exfoliated  $\text{WO}_3$  and  $\text{g-C}_3\text{N}_4$  ultrathin nanosheets develops high-quality interfacial contact, as confirmed by the atomic force microscopy images. Figure 6a-d shows microscale lateral size thickness of  $\text{WO}_3$  and  $\text{g-C}_3\text{N}_4$ , i.e., 3.0 nm and 2.5 nm, respectively, contributing to the strong electrostatic interfacial adherence  $\text{WO}_3$  and  $\text{g-C}_3\text{N}_4$ . This intimacy in ultrathin 2D  $\text{WO}_3/\text{g-C}_3\text{N}_4$  heterojunction fastens the surface photocatalytic reaction rate as photogenerated electrons and holes on heterogenous interface rapidly migrate to the surface of photocatalysts. Noteworthy, the thin layered structures of  $\text{WO}_3$  and  $\text{g-C}_3\text{N}_4$  and the strong coulombic forces enhanced the generation of internal electric

field (Fig. 6e-g) oriented from reductive type  $\text{g-C}_3\text{N}_4$  photocatalyst with  $\phi$  (4.18 eV) to oxidative  $\text{WO}_3$  with larger  $\phi$  of 6.23 eV. The upward band edge bending in  $\text{g-C}_3\text{N}_4$  improved its reduction ability for  $\text{O}_2^{\cdot-}$  release, while the participation of  $\cdot\text{OH}$  is an outcome of downward band bending in  $\text{WO}_3$ . The electron paramagnetic resonance and X-ray photoelectron spectroscopy results were in accordance with the charge transfer route to be the S-scheme mechanism by the presence of conduction band electrons in  $\text{g-C}_3\text{N}_4$  and valence band holes in  $\text{WO}_3$  (Fu et al. 2019). The atomic force microscopy characterization displays the nature of interfacial intimacy in heterojunction, favoring reducing charge migration distance and a much longer lifetime of the photoexcited charges.

### Internal electric field theoretical simulations

The internal electric field is generated due to the uneven distribution of electrons and holes and the difference in  $\phi$  between oxidation photocatalyst and reduction photocatalyst. The internal electric field determines the separation of the electron-hole pairs in the S-scheme photocatalytic system. Thereby, it is imperative to investigate the accelerated charge separation due to internal electric field through density functional theory computational studies, which provide high precision of electronic structure, bandgap tuning, and carrier mobilities of heterojunction photocatalysts. A

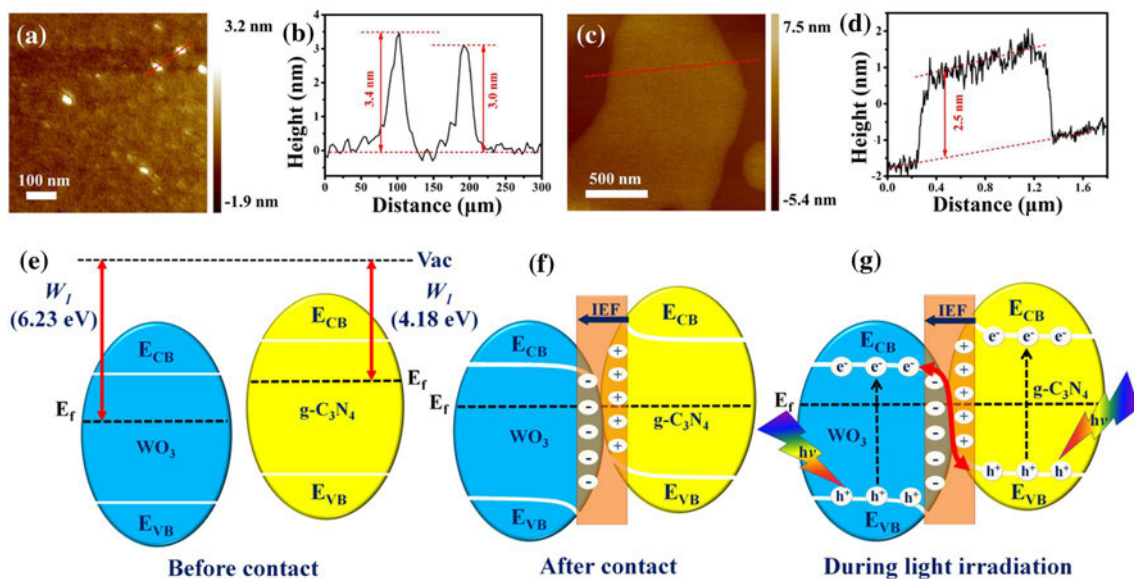


**Fig. 6** Atomic force microscopic images of: **a** and **b**  $\text{WO}_3$  nanosheets and **c** and **d**  $\text{g-C}_3\text{N}_4$  nanosheets representing the development of high-quality interfacial contact. Reproduced with permission (Fu et al. 2019). Copyright 2019, Elsevier. Diagrammatic illustration of **e** the band structure with different work functions ( $W_1$  and  $W_2$ ) of  $\text{WO}_3$  and  $\text{g-C}_3\text{N}_4$  before contact, **f** generation of the interfacial built-in electric field after contact and **g** S-scheme charge transfer route under

the exposure of light. The difference in the work function of  $\text{WO}_3$  and  $\text{g-C}_3\text{N}_4$  resulted in the diffusion of charge carriers with subsequent generation of the internal electric field leading to efficient reassembly of oppositely charged carriers at the interface of  $\text{WO}_3$  and  $\text{g-C}_3\text{N}_4$  forming an S-scheme heterojunction system. Adapted with permission (Fu et al. 2019). Copyright 2019, Elsevier

good illustration of the underlying S-scheme mechanism was observed in  $\text{NiO/BiOI}$  heterojunction by Fermi level estimation through density functional theory studies (Fig. 7a, b). According to the calculation results, the Fermi level of  $\text{BiOI}$  (110) is 6.364 eV, slightly larger than 6.327 eV of  $\text{NiO}$  (200), indicating electron migration from  $\text{NiO}$  to  $\text{BiOI}$  followed by generation of the internal electric field towards  $\text{BiOI}$  and band-edge bending. Under the effect of the internal electric field (Fig. 7c), conduction band electrons of  $\text{NiO}$  and holes from  $\text{BiOI}$  tend to recombine on the junction interface while restricting the  $\text{e}^-$  migration from  $\text{NiO}$  to  $\text{BiOI}$  in their conduction band. Simultaneously, electrons in the conduction band of  $\text{NiO}$  with  $-0.35$  eV and valence band holes of  $\text{BiOI}$  (2.36 eV) degraded rhodamine B dye.

This electron diffusion route was confirmed by shifts in binding energies of X-ray photoelectron spectroscopy peaks by 0.5 and 0.1 eV for  $\text{Ni } 2\text{p}_{3/2}$  and  $\text{Ni } 2\text{p}_{1/2}$  in 10%  $\text{NiO/BiOI}$  (BN10) composite. For  $\text{Bi } 4\text{f}_{7/2}$  and  $\text{Bi } 4\text{f}_{5/2}$  peaks, the BN10 sample exhibited  $\sim 0.3$  eV shifts towards lower binding energies compared to bare  $\text{BiOI}$ , while in  $\text{O } 1\text{ s}$  peak of ( $\text{Bi-O}$  and  $\text{Ni-O}$  bonds) BN10, the observed shifts were  $-0.2$  eV and  $0.2$  eV than pure  $\text{BiOI}$  and  $\text{NiO}$ . In contrast,  $\text{I } 3\text{d}_{5/2}$  and  $\text{I } 3\text{d}_{3/2}$  peaks of  $\text{I } 3\text{d}$  displayed no shifts in peaks for  $\text{BiOI}$  and BN10 samples (Hu et al. 2020). Likewise,  $\phi$  analysis was explored for  $\text{TiO}_2/\text{CdS}$  S-scheme heterojunction by density functional theory calculations. The lower  $\phi$  of  $\text{CdS}$  (5.91 eV) directs an internal electric field and

electron transference towards  $\text{TiO}_2$  (7.18 eV) to equilibrate the  $E_f$ . The direction of the internal electric field successfully prevents the recombination of high redox ability electrons in the conduction band of  $\text{CdS}$  and holes of  $\text{TiO}_2$ , making them available for photocatalytic  $\text{H}_2$  evolution reactions (Ge et al. 2019). These simulation results indicate that S-scheme charge-carrier migration is intrinsically feasible over traditional heterojunction mechanisms.

## Advantages of S scheme heterojunctions over traditional photocatalytic systems

The photocatalysis process has deep-rooted exponential growth due to the development of various heterojunctions. Among them, type-II and Z-scheme are hotly tipped two research areas in advanced photocatalysis (Kumar et al. 2020; Raizada et al. 2021; Xu et al. 2018). However, a deeper understanding of both mechanisms has revealed the inherent drawbacks of traditional photocatalytic systems, reducing photocatalytic efficiency. With the type-II charge transfer route, it is not easy to achieve the targeted charge separation, and the overall redox power of photocatalysts is undermined (Sudhaik et al. 2020a). For instance, in the  $\text{TiO}_2\text{-MoS}_2$  type-II charge migration route, Wang et al. claimed  $\cdot\text{OH}$  radical as the major reactive species produced via transference of holes from a more positive 2.99 eV valence band of  $\text{TiO}_2$

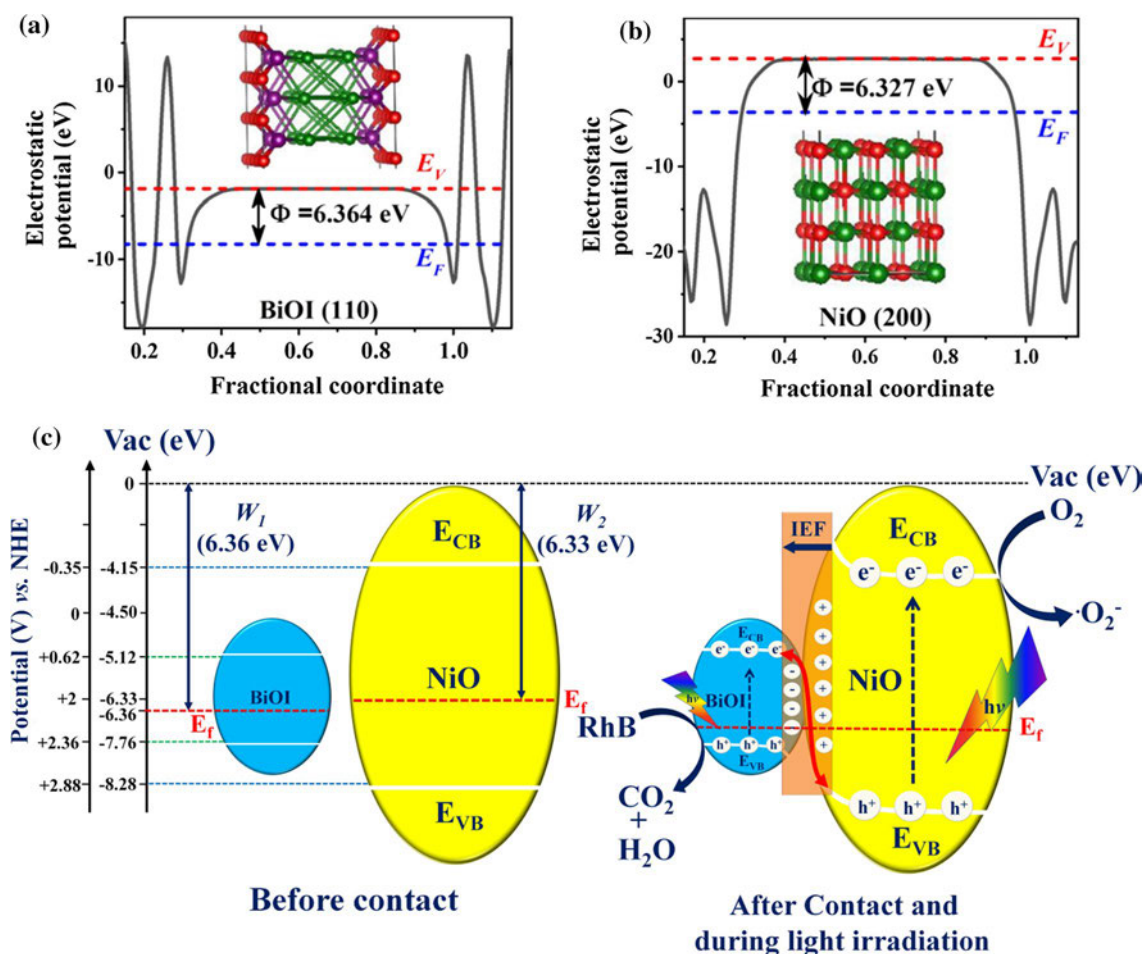


**Fig. 7** Calculated electrostatic potentials for **a** (110) face of BiOI and **b** (200) face of NiO with the respective difference in the work function ( $\Phi$ ) values of both BiOI and NiO. Reproduced with permission (Hu et al. 2020). Copyright 2020, Elsevier. **c** The mechanistic view of the charge migration route followed by NiO/BiOI heterojunction before contact and after contact. After an intact contact between BiOI and NiO, the induced internal electric field at the interface facilitated

the reassembly of useless charge carriers and promoted the isolation of photocarriers with high redox potential through S-scheme charge transfer mode (the symbols  $W_1$ ,  $W_2$ , and  $Vac$  represent work function of BiOI, a work function of NiO and vacuum energy levels, respectively). Adapted with permission (Hu et al. 2020). Copyright 2020, Elsevier

to lesser positive 1.825 eV  $MoS_2$  valence band as shown in (Fig. 8a). However, it is difficult to ascertain the mechanism of  $\cdot OH$  radical generation by  $MoS_2$  even though it lacks the minimum potential required, i.e.,  $E^\circ (\cdot OH/H_2O)$  is 1.99 V, and  $E^\circ (\cdot OH/OH^-)$  is 2.8 V (Wang et al. 2016). The charge transference process also decreases the reductive and oxidative potentials of electrons and holes.

Hence, a closer inspection of the type-II heterojunction mechanism is debatable and neglects the primary redox potential criteria for reactive oxidative species generation. However, authentic charge carrier migration route has been proposed in the S-scheme  $TiO_2$ - $W_{18}O_{49}$  heterojunction (Fig. 8b), where built-in internal electric field directed from  $TiO_2$  to  $W_{18}O_{49}$  resulted in upward and downward band bending, respectively. The effective charge carrier separation was obtained on the recombination of useless

photogenerated electrons of  $W_{18}O_{49}$  and holes of  $TiO_2$  with the eventual release of  $O_2^{\cdot-}$  via photoinduced conduction band electrons of  $TiO_2$ . If the charge carriers followed the type-II mechanism rather than S-scheme, the photoinduced conduction band electrons of  $TiO_2$  would be transferred to the conduction band of  $W_{18}O_{49}$ , nullifying the generation of  $O_2^{\cdot-}$  radicals (Wang, R. et al. 2020).

Consequently, fabrication of traditional Z-scheme photocatalytic system with shuttle redox ion pairs, all-solid-state electron mediators, and direct Z-scheme emerged from biomimicking artificial photosynthesis process (Zhou et al. 2014). Although Z-scheme heterojunction tends to resolve the quandaries of simultaneously attaining minimal charge carrier separation and higher redox potentials, it has limitations (Jiang et al. 2018). The aqueous shuttle redox-mediated Z-scheme system has restricted applicability



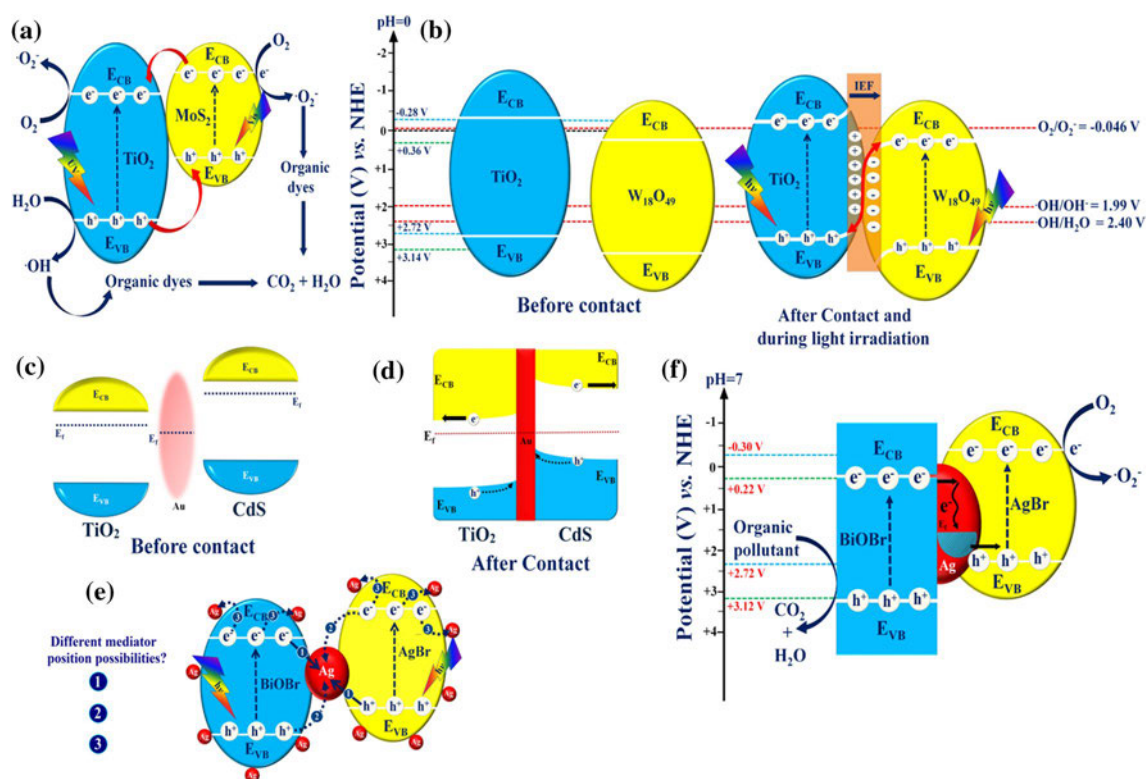


**Fig. 8** **a** Band diagram showing type-II charge transfer mode in TiO<sub>2</sub>-MoS<sub>2</sub> heterojunction for the removal of organic dyes. Adapted with permission (Wang et al. 2016). Copyright 2016, Elsevier. **b** Schematic illustration representing the internal electric field promoted S-scheme charge transfer mode in TiO<sub>2</sub>-W<sub>18</sub>O<sub>49</sub> heterojunction after contact under the illumination of visible light. Adapted with permission (Wang, R. et al. 2020). Copyright 2020, Elsevier. Schematics representing: **c** band diagrams with Fermi level positioning in TiO<sub>2</sub>, Au and CdS, **d** band-bending due to charge redistribu-

tion in CdS-Au-TiO<sub>2</sub> all-solid-state Z-scheme system, and **e** possible attachment sites of Au nanoparticles on TiO<sub>2</sub> and CdS photocatalysts. Adapted with permission (Xu et al. 2020), Copyright 2020, Cell Press. **f** Charge transfer process in AgBr/BiOBr all-solid-state Z-scheme heterojunction with Ag nanoparticles as electron transfer mediator with surface plasmon effect promoting the migration and isolation photocarriers. Adapted with permission (Ye et al. 2012). Copyright 2012, American chemical society

due to functioning in only liquid phase, pH sensitivity, and backward reactions, which inevitably reduces the number of available charge carriers photocatalytic reactions (Wang et al. 2018; Xia et al. 2019). All-solid-state Z-scheme eliminates the usage of redox couples by replacing them with a solid-state mediator as an electron transference bridge (Natarajan et al. 2018).

In 2006, Tada et al. reported Au as a solid-state electron mediator, which helped in space charge isolation by utilizing left out electrons in the conduction band of TiO<sub>2</sub> and holes in the valence band of CdS (Tada et al. 2006). However, the asserted charge transfer process in CdS-Au-TiO<sub>2</sub> all-solid-state Z-scheme does not obey the perspective of Fermi levels and band bending. (Fig. 8c) depicts Fermi level positions before contact, where CdS has a higher Fermi level than TiO<sub>2</sub> and Au has the lowest, whereas, after coming into direct contact (Fig. 8d), the Fermi level aligns owing to the redistribution of charge carriers at the interface resulting in upward band bending. Consequently, the electron flow from

CdS and TiO<sub>2</sub> to Au will be inhibited due to the formation of Schottky barriers at the interface. Therefore, the reported charge-carrier transference involving the reassembly of TiO<sub>2</sub> electrons with holes of CdS is not feasible.

The controlled synthesis process to optimally obtain the geometrical position of the solid conductor in between two photocatalysts is highly uncertain. For instance, in AgBr/BiOBr all-solid-state Z-scheme heterojunction, Ag nanoparticles served as electron mediators as presented in (Fig. 8e). The charge migration mechanism leads to the generation of O<sub>2</sub><sup>•-</sup> by a flow of photoexcited electrons from BiOBr into the Ag nanoparticles through the Schottky barrier as the conduction band of BiOBr (+0.22 eV) is more negative than the Fermi level of Ag. Simultaneously, there is a migration of valence band holes of AgBr into Ag since the Fermi level of Ag is more positive than the valence band of AgBr (+2.30 eV). The claimed all-solid-state Z-scheme charge transfer route is considerate of Fermi levels but is possible only when Ag metal is sandwiched between AgBr and

BiOBr (Ye et al. 2012). However, it is difficult to guarantee that a solid conductor lies exactly in-between two photocatalysts (Fig. 8f).

There is a high probability of random adherence of solid conductors onto the surface of photocatalysts, which alters their functionality from electron mediators to act as co-catalysts (Di et al. 2019; Huang et al. 2019). In addition to the above drawbacks, noble metal nanoparticles and carbonaceous conductors often suffer from light-shielding effects due to their substantial absorption in the visible and near-infrared region (Li et al. 2016). Consequently, the all-solid-state Z-scheme photocatalytic system is unsatisfying and rendered evolution of mediator-free Z-scheme since Yu et al. proposed the concept of direct Z-scheme system involving  $\text{TiO}_2$  and  $\text{g-C}_3\text{N}_4$  photocatalysts (Yu et al. 2013). However, the insufficiency of characterization techniques to ascertain the direct Z-scheme mechanism makes it ambiguous and vulnerable as it belongs to the family of problematic traditional and all-solid-state Z-scheme (Xu et al. 2020; Zhang, W. et al. 2020). A paradigm shift from traditional type-II to Z-scheme and the current S-scheme photocatalytic system provides the benefits of mechanistic interpretation depicting S-scheme charge migration's superiority and subsequent retention in redox ability of the system.

## Strategies for constructing S-scheme photocatalysts

The collaborative attainment of both reaction thermodynamics and dynamics of S-scheme heterojunction is still in its infancy. Although the thermodynamics factor (Ohtani, 2014), i.e., overcoming the activation barrier for effective charge migration, is favorable, the dynamics issue of S-scheme photocatalysts is insufficient. To further ameliorate the photocatalytic performance of S-scheme heterojunctions for water splitting,  $\text{H}_2$  evolution, pollutant degradation, and  $\text{CO}_2$  reduction, the following parameters should be scrutinized.

- Typically, photocatalytic water splitting and  $\text{CO}_2$  reduction are thermodynamically uphill processes and exhibit positive Gibbs free energy ( $\Delta G > 0$ ) acting as an activation barrier. In contrast, photocatalytic pollutant degradation is a thermodynamically downhill reaction ( $\Delta G < 0$ ) (Ohtani, 2010). This variance in the thermodynamics aspect can be overcome by co-catalyst dispersion on the photocatalytic surface. The most commonly employed co-catalysts are noble metal-free (Pt, Au, Ag, etc.) (Bai et al. 2014; Li et al. 2019) with merits of high mobility of charge carriers, light transparency, and large density of active sites photocatalytic applications (Xia, Y. et al. 2020).

- The appropriate band alignment of heterojunction photocatalysts is required to release reactive oxidative species, and a bandgap lower than 3.0 eV leads to improved visible light-harvesting (Patnaik et al. 2021). One of the promising approaches for this is morphology control involving non-metal doping, i.e., N, S, and O are introduced at the atomic level to improve the inherent optical and electronic features (Jiang et al. 2017). It is assumed that dopants form localized states between the  $E_g$  limits, impacting conduction band minima and valence band maxima edges.
- The surface capacity of photocatalysts involving surface area and available active sites are imperative for solar energy conversion efficiency. The overlapping band potentials of oxidation photocatalyst and reduction photocatalyst provide intimate contact and broader surface area for the recombination of useless electron-hole pairs. This design is possible via sufficient contact between two-dimensional (2D/2D) interfacial surface contact. Plenty of face-face 2D heterojunction has been used, such as  $\text{MoS}_2/\text{CdS}$  (Yuan et al. 2018),  $\text{ZnIn}_2\text{S}_4/\text{g-C}_3\text{N}_4$  (Qin, Y. et al. 2020),  $\text{TiO}_2/\text{g-C}_3\text{N}_4$  (Zhang, Y. et al. 2020), and  $\text{g-C}_3\text{N}_4\text{-In}_2\text{Se}_3$  (Zhang, S. et al. 2020), etc.

## Co-catalyst loading

The strong interfacial electronic interactions between co-catalyst-semiconductor assure enhanced photocatalytic activity by overcoming a large activation barrier of the photocatalytic surface for the reaction molecules (Tong et al. 2020). In S-scheme heterojunctions, co-catalysts attached with the oxidation photocatalyst/reduction photocatalyst extract the charges out of the photocatalytic surface and serve as active sites for molecule oxidation and reduction. Notably, co-catalyst integration helps extend the charge carrier lifetime, alteration in the flat band potential, and Fermi level (Xiao et al. 2020).

A clear insight into the role of metal-free co-catalysts was revealed in ternary  $\text{SnNb}_2\text{O}_6/\text{CdS}$ -diethyltri-amine, co-catalyzed by  $\text{Ni}_2\text{P}$ . The well-defined S-scheme charge transfer route (Fig. 9a) led to a built-in-internal electric field formation with a transference of photogenerated electrons from the conduction band of  $\text{SnNb}_2\text{O}_6$  to  $\text{Ni}_2\text{P}$  co-catalyst. The ultrathin sheet-like morphology with a thickness of 1.5 nm obtained via field emission scanning electron microscopy and atomic force microscopy images increased the available surface area for  $\text{H}_2$  evolution. This was confirmed by Brunauer–Emmett–Teller isotherm results where the improved surface area of  $93.72 \text{ m}^2/\text{g}$  was obtained for 10%  $\text{SnNb}_2\text{O}_6/\text{CdS}$ -diethyltri-amine/ $\text{Ni}_2\text{P}$ , much larger than  $36.89 \text{ m}^2/\text{g}$  of bare  $\text{SnNb}_2\text{O}_6$  and  $87.63 \text{ m}^2/\text{g}$  of  $\text{CdS}$ -diethyltri-amine. During the photocatalytic process, the Schottky junction between  $\text{SnNb}_2\text{O}_6$  and  $\text{Ni}_2\text{P}$  promoted  $\text{H}_2$  evolution up



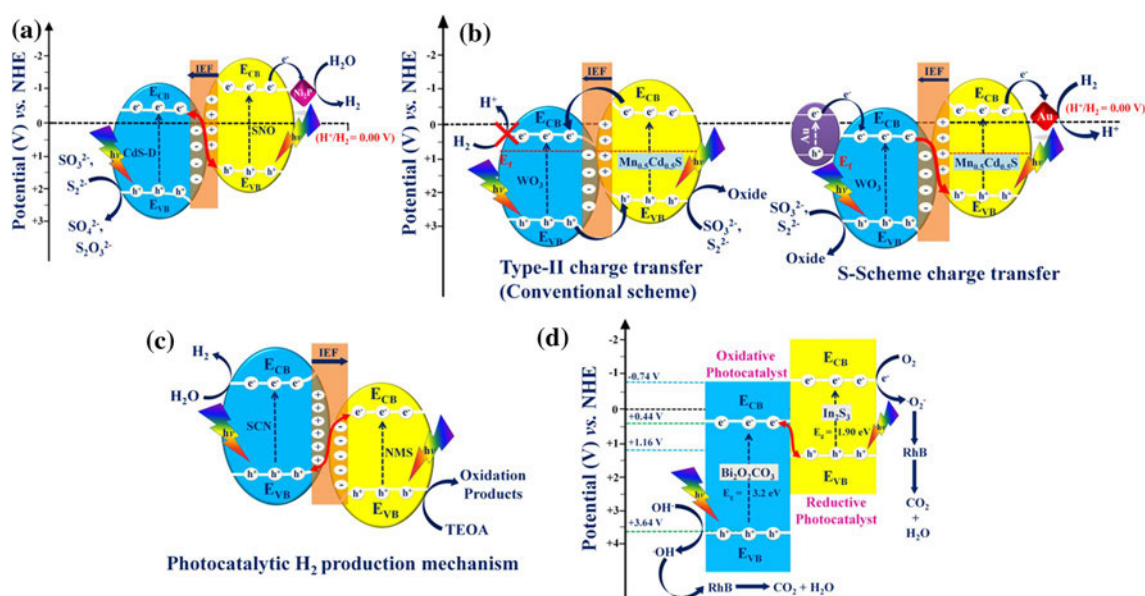


**Fig. 9** a Band diagram showing S-scheme charge transfer route in  $\text{SnNb}_2\text{O}_6/\text{CdS-D}/\text{SNO}$  photocatalytic system co-catalyzed by  $\text{Ni}_2\text{P}$ . The charge redistribution followed by the generation of internal electric field promoted the S-scheme mechanism, and  $\text{Ni}_2\text{P}$  co-catalyst further enhanced the isolation and participation of photocarriers in surface-induced catalytic reactions. Adapted with permission (Hu, T. et al. 2020). Copyright 2020, Elsevier. b Schematics illustrating the possible S-scheme charge transfer pathway followed by  $\text{Mn}_{0.5}\text{Cd}_{0.5}\text{S}/\text{WO}_3$  system over conventional type-II heterojunction system promoted by Coulombic interactions, internal electric field, and band edge bending. Adapted with permission (Liu et al. 2020). Copyright 2020, Elsevier. c Diagrammatic illustration

of  $\text{H}_2$  production mechanism shown by N-doped  $\text{MoS}_2$  (NMS) and S-doped  $\text{g-C}_3\text{N}_4$  (SCN) S-scheme heterojunction system. Under the influence of the internal electric field, the photoinduced electrons in the conduction band of SCN and photoinduced holes in the valence band of NMS with strong redox ability were preserved to participate in photoredox reactions. Adapted with permission (Chen et al. 2021). Copyright 2021, Elsevier. d Band diagram with respective band edge potentials and bandgap energy showing possible S-scheme charge transfer route in  $\text{In}_2\text{S}_3/\text{Bi}_2\text{O}_2\text{CO}_3$  heterojunction system for photocatalytic degradation of rhodamine B (RhB). Adapted with permission (Fan et al. 2020). Copyright 2020, Elsevier

to  $11,992 \mu\text{mol g}^{-1} \text{h}^{-1}$  from the active sites of  $\text{Ni}_2\text{P}$ , much higher than  $60, 3319, 7808 \mu\text{mol g}^{-1} \text{h}^{-1}$  obtained over bare  $\text{SnNb}_2\text{O}_6$ ,  $\text{CdS}$  and  $10\%-\text{SnNb}_2\text{O}_6/\text{CdS}$ -diethyltriamine, respectively (Hu, T. et al. 2020).

Noble metal-based co-catalyst such as Au deposited on  $\text{Mn}_{0.5}\text{Cd}_{0.5}\text{S}/\text{WO}_3$  S-scheme heterojunction (Fig. 9b) facilitates recombination of conduction band electrons of  $\text{WO}_3$  and valence band holes of  $\text{Mn}_{0.5}\text{Cd}_{0.5}\text{S}$  under the influence of Coulombic interactions, internal electric field, and band edge bending. This was a well-in agreement with photoluminescence spectra, transient photocurrent response, and electrochemical impedance spectroscopy measurements jointly signify the charge separation efficiency in the order of  $\text{Mn}_{0.5}\text{Cd}_{0.5}\text{S}/\text{WO}_3/\text{Au} > \text{Mn}_{0.5}\text{Cd}_{0.5}\text{S}/\text{WO}_3 > \text{bare Mn}_{0.5}\text{Cd}_{0.5}\text{S}$ . Based on the density functional theory computational studies, Au co-catalyst with  $\phi$  5.1 eV transfers its electrons to  $\text{WO}_3$  (6.23 eV) due to the surface plasmon resonance effect extending a broad absorption peak around 530 nm (Liu et al. 2020). The dual advantages of co-catalyst deposition are accelerated charge carrier migration by serving as electron trappers and boosted solar energy absorption.

## Bandgap tuning

The bandgap adjustment in S-scheme heterojunction is imperative to accelerate the separation of the electron-hole pairs, enhances the redox abilities, and broadens the solar spectrum absorption simultaneously. Fortunately, incorporating a metallic/non-metallic dopant has been a promising strategy in improving photocatalytic efficiency (Sushma and Kumar, 2017). The orbital hybridization between the dopant and host orbital leads to modification in an electronic structure and redox potentials of the conduction band and valence band (Hasija et al. 2019). This was evinced in the S-scheme heterojunction formed by  $\text{TiO}_2$  and S-doped  $\text{g-C}_3\text{N}_4$ , where the bandgap of bare  $\text{g-C}_3\text{N}_4$  was lowered from 2.67 to 2.43 eV after S doping. The other benefits of S-doped  $\text{g-C}_3\text{N}_4$  include redshift photoabsorption up to 510 nm and increment in active sites due to increased surface area of  $51 \text{ m}^2/\text{g}$  from  $16 \text{ m}^2/\text{g}$  for  $\text{TiO}_2/\text{S-doped g-C}_3\text{N}_4$  and bare  $\text{TiO}_2$ , respectively (Wang et al. 2021).

Similar observations were obtained in a study involving N-doped  $\text{MoS}_2$  coupled with S-doped  $\text{g-C}_3\text{N}_4$  S-scheme heterojunction; there was a generation of more active edge sites on replacement of S atom with N atom in  $\text{MoS}_2$  as revealed

in X-ray photoelectron spectroscopy spectra. The interfacial interactions between N-doped MoS<sub>2</sub> and S-doped g-C<sub>3</sub>N<sub>4</sub> were investigated by density functional theory calculations (Fig. 9c). There was a reduction in the  $\phi$  of bare g-C<sub>3</sub>N<sub>4</sub> and MoS<sub>2</sub> from 4.67 and 5.96 eV to 3.78 and 5.57 eV, respectively, upon incorporating S and N atoms. Moreover, dopants lowered the bandgap from 2.80 eV to 2.56 eV and reduced the potential for H<sub>2</sub> evolution. The doped heterojunction resulted in 658.5  $\mu\text{mol g}^{-1} \text{h}^{-1}$ , whereas only 28.8 and 17.4  $\mu\text{mol g}^{-1} \text{h}^{-1}$  were obtained for bare N-doped MoS<sub>2</sub> and S-doped g-C<sub>3</sub>N<sub>4</sub>, respectively (Chen et al. 2021). Ionic doping has a profound effect on the band structure and photocatalytic efficiency.

## Interfacial optimization

The appropriate intimacy between oxidation photocatalyst and reduction photocatalyst in S-scheme heterojunction plays a vital role in effective charge-carrier migration/separation and enhancing the redox capability of the high potential conduction band and valence band under light illumination (Sakthivel et al. 2019). The face-to-face 2D/2D heterojunction between In<sub>2</sub>S<sub>3</sub>/Bi<sub>2</sub>O<sub>2</sub>CO<sub>3</sub> not only extended the absorption to 600 nm but also restrained the recombination of useful photoexcited electron-hole pairs, as demonstrated in the S-scheme mechanism (Fig. 9d). Upon illumination of light, the internal electric field was directed from In<sub>2</sub>S<sub>3</sub> to Bi<sub>2</sub>O<sub>2</sub>CO<sub>3</sub>, i.e., from higher to lower Fermi level. Subsequently, weak reductive electrons from the conduction band of Bi<sub>2</sub>O<sub>2</sub>CO<sub>3</sub> recombined with the weak oxidative valence band holes of In<sub>2</sub>S<sub>3</sub>. The enhanced release of O<sub>2</sub><sup>•-</sup>, holes, <sup>•</sup>OH from the conduction band of In<sub>2</sub>S<sub>3</sub> (− 0.74 eV) and valence band of Bi<sub>2</sub>O<sub>2</sub>CO<sub>3</sub> (3.64 eV), respectively, was confirmed by active species trapping experiment results. The graphical result revealed a decline in rhodamine B dye degradation rate on the addition of scavengers in the following trend; Na<sub>2</sub>Cr<sub>2</sub>O<sub>4</sub> > benzoquinone > isopropanol in 10% In<sub>2</sub>S<sub>3</sub>/Bi<sub>2</sub>O<sub>2</sub>CO<sub>3</sub>. Meanwhile, the scanning electron microscopy images indicate the aggregation of 2D Bi<sub>2</sub>O<sub>2</sub>CO<sub>3</sub> nanosheets stacked over 2D In<sub>2</sub>S<sub>3</sub> nanosheets with an atomic thickness of 3–5 nm, which offers the quick charge migration pathway and rich active sites for surface photocatalytic reactions (Fan et al. 2020).

Another advantage obtained by 2D-2D S-scheme interfacial charge transfer route was higher charge carrier lifetime, as studied by Huo et al. in porous carbon nitride/bismuth oxychloride heterojunction obtained via annealing at 450 °C (Huo et al. 2021). The Bode plot revealed a twofold increase in charge carrier lifetime in porous carbon nitride/bismuth oxychloride – 450 i.e., 109 ms much higher than 16, 33, 54 ms of bare porous carbon nitride, bismuth oxychloride, and porous carbon nitride/bismuth oxychloride, respectively, indicative of effective separation of photogenerated charge

carriers. This was evident in a plausible S-scheme mechanism, which resulted in the formation of a space charge region due to the electron density difference between porous carbon nitride and bismuth oxychloride. The downward band bends in bismuth oxychloride resulted in a generation of accumulation layer with the synchronous formation of the depletion layer near the porous carbon nitride interface. Under the influence of the internal electric field, the electrons of bismuth oxychloride combined with holes of porous carbon nitride with simultaneous suppression in the recombination of electrons of porous carbon nitride and holes of bismuth oxychloride.

## Photocatalytic applications

### Water splitting

The application of hybrid photocatalysts for solar-driven H<sub>2</sub> and O<sub>2</sub> production from water in the presence or absence of an electron scavenger has intensely emerged. Undoubtedly, photocatalytic water splitting is a green and environment-friendly approach to store and convert solar energy into valuable fuels such as H<sub>2</sub>. However, for a convincing overall water splitting process, the photocatalytic efficiency of the system critically depends upon the band alignment (appropriate conduction band and valence band edge potential with sufficient redox potentials), optical absorption, spatial isolation of photocarriers, and availability of abundant active sites. In terms of thermodynamics, the uphill reaction kinetics of overall water splitting requires a photocatalyst must possess a wide enough bandgap energy (> 1.23 eV) to overcome + 237.2 kJ mol<sup>−1</sup> of Gibbs free energy. Thus, broad bandgap energy (> 1.6 eV) is required to compensate for the additional over potential linked with the electron transference and gas evolution steps (Liras et al. 2019; Xu et al. 2018).

Of note, a single photocatalytic system cannot fulfill all the counteractive requirements associated with the water-splitting process. Thus, exploring new photocatalytic systems in combination with classical ones that satisfy all necessary aspects is highly desirable. Fortunately, the newly developed S-scheme heterojunction systems display a substantial potential to achieve superior photocatalytic performance due to effective space charge separation and improved redox ability. For instance, Zhang et al. reported a binary Bi<sub>2</sub>S<sub>3</sub>/g-C<sub>3</sub>N<sub>4</sub> S-scheme heterostructure formed through a facile one-step solvent-assisted route for photo-assisted H<sub>2</sub> evolution (Zhang et al. 2021). The optimized Bi<sub>2</sub>S<sub>3</sub>/g-C<sub>3</sub>N<sub>4</sub> sample with 0.6% loading of Bi<sub>2</sub>S<sub>3</sub> (1D nanorods) onto g-C<sub>3</sub>N<sub>4</sub> (2D nanosheets) exhibited an exceptional H<sub>2</sub> production rate of 3394.1  $\mu\text{mol g}^{-1} \text{h}^{-1}$ . Based on the radical trapping experiment and bandgap analysis results in the typical

S-scheme charge transfer mode (Fig. 10a-c) was proposed, which facilitated space charge isolation while improving the redox ability of the system. After contacting, the Fermi levels of oxidative  $\text{Bi}_2\text{S}_3$  and reductive  $\text{g-C}_3\text{N}_4$  were aligned, leading to band-bending, which facilitated the recombination of useless electrons in the conduction band of  $\text{Bi}_2\text{S}_3$  with the holes in the valence band of  $\text{g-C}_3\text{N}_4$ .

Thus, the electrons and holes with superior redox potentials were available for their participation in photocatalytic  $\text{H}_2$  production reactions. The selection of semiconductor material with suitable band edge positioning plays a crucial role in constructing an S-scheme photocatalyst. In that regard, utilizing molybdenum oxide with abundant O-vacancies ( $\text{MoO}_{3-x}$ ) exhibits intense and broad range localized surface plasmon resonance absorption around 700 nm, enhancing the absorption towards near-infrared region beneficial for  $\text{H}_2$  evolution reaction. Thus, decorating 0D CdS nanoparticles onto plasmonic 2D  $\text{MoO}_{3-x}$  nanosheets via simpler co-precipitation method rendered a 0D/2D CdS/ $\text{MoO}_{3-x}$  S-scheme heterostructure with improved charge-carrier separation kinetics and enhanced rate of  $\text{H}_2$  production ( $7.44 \text{ mmol} \cdot \text{g}^{-1} \cdot \text{h}^{-1}$ , 10.3 times higher than pristine CdS) (Peng et al. 2021). Combined results from X-ray photoelectron spectroscopy and density functional theory

studies demonstrated that after an intact junction, an internal field was established between CdS (positively charged) and  $\text{MoO}_{3-x}$  (negatively charged) resulted in upward and downward band-bending of CdS and  $\text{MoO}_{3-x}$ , respectively (Fig. 10d-f). Thus, broad light absorption provided through plasmonic effect endowed superior generation of charge carriers, which were spatially migrated due to induced electric field and band-bending. As a consequence, the hot electrons accumulated on the conduction band of  $\text{MoO}_{3-x}$  were recombined with the holes in the valence band of CdS, rendering powerful electrons in the conduction band at CdS to promote photo-assisted water-splitting reaction.

The criteria of intact interfacial contact and matched bandgap alignments of adjoining semiconductor photocatalysts remarkably affect the spatial isolation of charge carriers boosted by the induced internal electric field. Thus, combining suitable photocatalysts with an effective interfacial junction is another alluring approach for attaining superior charge isolation kinetics. Tao et al. fabricated 2D CoAl layered double hydroxide and 2D  $\text{MoS}_2$  S-scheme photocatalyst with a remarkably enhanced internal electric field for ameliorated  $\text{H}_2$  production rate (by optimized  $\text{MoS}_2/\text{CoAl}$  layered double hydroxide composite) of  $17.1 \mu\text{mol} \cdot \text{g}^{-1} \cdot \text{h}^{-1}$  (Tao et al. 2021). The calculated  $\phi$  (from density functional

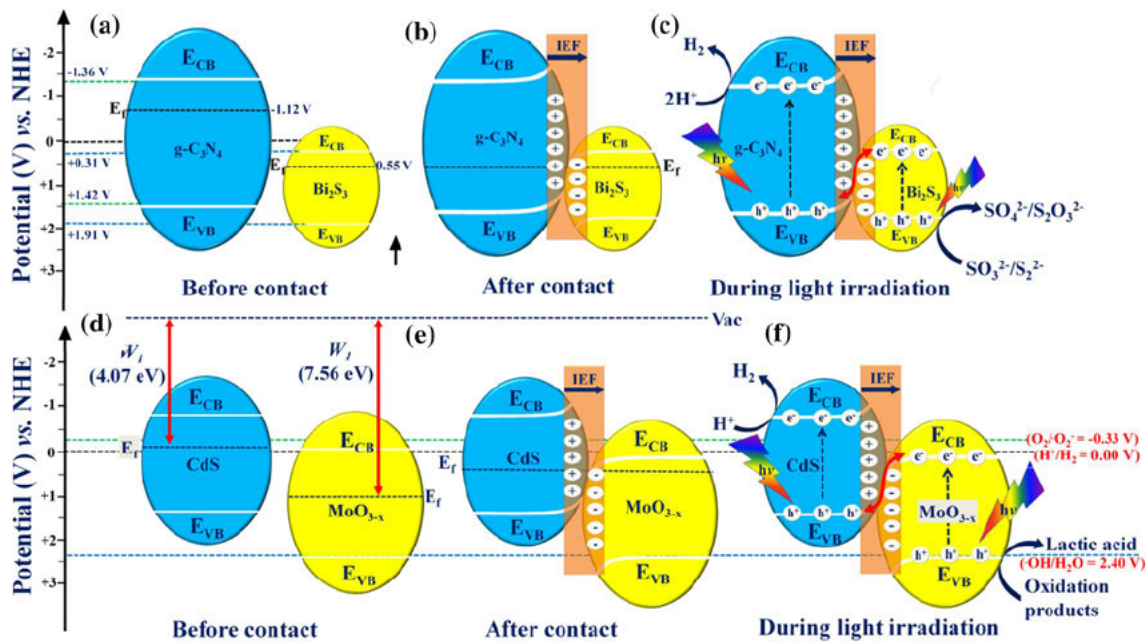


**Fig. 10** S-scheme charge transfer mode in  $\text{Bi}_2\text{S}_3/\text{g-C}_3\text{N}_4$  heterojunction in three stages **a** before contact **b** after contact, and **c** under the illumination of light. After contact, due to the redistribution of charges the interfacial built-in electric field was produced, which promoted the recombination of useless charge carriers at the interface of  $\text{Bi}_2\text{S}_3$  and  $\text{g-C}_3\text{N}_4$  and preserved the photocarriers with high redox potential for photocatalytic reactions. Adapted with permission (Zhang et al. 2021). Copyright 2021, Elsevier. Band diagrams with

respective band edge potentials and Fermi energy levels ( $E_f$ ) showing: **d** respective work functions ( $W_1$  and  $W_2$ ) of CdS and  $\text{MoO}_{3-x}$  before contact, **e** formation of depletion layer and built-in internal electric field after contact, and **f** possible S-scheme charge transfer pathway followed by CdS/ $\text{MoO}_{3-x}$  heterostructure resulting in efficacious migration and isolation of photocarriers. Adapted with permission (Peng et al. 2021). Copyright 2021, Elsevier



theory calculation) of CoAl and MoS<sub>2</sub> revealed the migration of electrons from CoAl layered double hydroxide (smaller  $\phi$ ) to MoS<sub>2</sub> (higher  $\phi$ ) after contact, which triggered the internal electric field from CoAl layered double hydroxide to MoS<sub>2</sub>. Upon visible light exposure and bending of energy levels induced by the internal electric field, the electrons in the conduction band of MoS<sub>2</sub> will recombine with the holes in the valence band of CoAl layered double hydroxide by following S-scheme charge transfer mode retained high reduction ability of the MoS<sub>2</sub>/CoAl-layered double hydroxide system beneficial for H<sub>2</sub> production reaction. As a whole, the photocatalytic water splitting performance can be smartly enhanced through S-scheme heterojunction formation between photocatalytic materials with suitable band edge positioning and different  $\phi$  values, which can stimulate the formation of the internal electric field for efficient isolation of photocarriers.

## CO<sub>2</sub> conversion

The controlled emission and mitigation of anthropogenic CO<sub>2</sub> is one of the major concerns which demand collective efforts. So far, the actions proposed for controlling the elevating CO<sub>2</sub> levels into the atmosphere mainly comprise CO<sub>2</sub> capture and valorization. To fulfill this substantial objective, one of the most desired and intriguing processes is the photo-assisted reduction of CO<sub>2</sub> into value-added fuels or chemicals (Kumar et al. 2021a; Mao et al. 2013). However, the exceptionally stable molecular structure of CO<sub>2</sub> (high C = O bond dissociation energy  $\sim 750$  kJmol<sup>-1</sup>) necessitates renewable energy sources to make the process more viable. The direct photoconversion of gaseous CO<sub>2</sub> is thermodynamically not feasible owing to the high negative CO<sub>2</sub>/CO<sub>2</sub><sup>-</sup> redox potential ( $-1.90$  V vs. NHE; normal hydrogen electrode), at pH = 7.0). Besides, proton-assisted CO<sub>2</sub> photoreduction seems a more promising approach prompted by relatively lower redox potential values. Consequently, the complex multi-electronic process of CO<sub>2</sub> photoreduction must overcome the activation barriers and thermodynamic feasibility involved in charge migration kinetics influenced by interfacial interactions between reagents and semiconductors.

In that regard, the construction of S-scheme heterostructures could be a fascinating strategy as it facilitates space charge isolation and retains the high redox ability suitable for effective CO<sub>2</sub> photoreduction. For instance, Xu et al. reported CsPbBr<sub>3</sub> quantum dots (QDs) decorated TiO<sub>2</sub> nanofibers (TiO<sub>2</sub>/CsPbBr<sub>3</sub>) constructed through a facile electrostatic self-assembly route for efficient CO<sub>2</sub> photoreduction into CO ( $9.02 \mu\text{mol g}^{-1} \text{h}^{-1}$ ) (Xu, F. et al. 2020). The randomly stacked TiO<sub>2</sub> nanofibres composed of small nanocrystals exhibit exposed active sites due to the loosely bound structure promoted the transportation of photocarriers and

adsorption-desorption kinetics of reactants and products. Therefore, such a unique assembly with increased surface area and exposed active sites can remarkably enhance CO<sub>2</sub> photoconversion efficiency. The experimental study involving ex situ X-ray photoelectron spectroscopy analysis and density functional theory calculation results supported the presence of internal electric field induced in TiO<sub>2</sub>/CsPbBr<sub>3</sub> heterojunction system, which expedited the spatial isolation of photocarriers via S-scheme mode as shown in (Fig. 11a-c). The in situ X-ray photoelectron spectroscopy spectra depicted positive shift (0.5 eV) in the binding energies of Ti 2p and O 1 s, while the negative shift (0.5 eV) in the binding energies of Cs 3d, Br 3d, and Pb 4f concerning the ex situ spectra under the exposure of UV-visible light verified the transfer of electrons in the conduction band of TiO<sub>2</sub> to the valence band of CdPbBr<sub>3</sub> QDs confirming the S-scheme mechanism.

In a unique study, p-type ZnMn<sub>2</sub>O<sub>4</sub> and n-type ZnO were coupled via electrospinning and calcination to form a hierarchical ZnMn<sub>2</sub>O<sub>4</sub>/ZnO heterojunction, which outperformed the bare ZnO photocatalyst with  $\sim 4$ -times increment in CH<sub>4</sub> and CO yields by following S-scheme charge transfer route (Deng et al. 2021). Through density functional theory calculations, it was observed that before contacting, the  $\phi$  of ZnMn<sub>2</sub>O<sub>4</sub> (4.55 eV) was smaller than that of ZnO (4.63 eV). After contacting due to the difference in  $\phi$  and Fermi energy values, the electrons in the conduction band of ZnMn<sub>2</sub>O<sub>4</sub> moved towards ZnO until their Fermi energy levels aligned equally; consequently, a depletion layer was formed between ZnMn<sub>2</sub>O<sub>4</sub> (positively charged) and ZnO (negatively charged). Thus, an internal electric field pointed from ZnMn<sub>2</sub>O<sub>4</sub> to ZnO formed the basis of efficient charge transfer through the S-scheme pathway leading to productive CO<sub>2</sub> photoconversion efficiency. Other than density functional theory calculations, X-ray photoelectron spectroscopy analysis also verified the S-scheme charge migration route followed by ZnMn<sub>2</sub>O<sub>4</sub>/ZnO heterojunction. The adsorption and activation of CO<sub>2</sub> molecules at the surface of photocatalyst play a critical role in ameliorating the CO<sub>2</sub> photoconversion phenomenon.

Polymeric g-C<sub>3</sub>N<sub>4</sub> enriched with N-containing functional groups is a fascinating material for photocatalytic CO<sub>2</sub> adsorption and subsequent reduction into energy-dense hydrocarbon fuels. Thus, constructing the S-scheme heterostructure of polymeric g-C<sub>3</sub>N<sub>4</sub> can efficiently suppress the reassembly of useful photocarriers required for the CO<sub>2</sub> photoreduction process. For instance, Mei et al. fabricated CoO/polymeric g-C<sub>3</sub>N<sub>4</sub> S-scheme heterojunction by developing in situ CoO on porous polymeric g-C<sub>3</sub>N<sub>4</sub>, which showed an improved rate of CO<sub>2</sub> photoconversion into CO ( $40.31 \mu\text{mol g}^{-1} \text{h}^{-1}$ ), which was 23.85 and 3.43 times superior to bare polymeric g-C<sub>3</sub>N<sub>4</sub> ( $1.69 \mu\text{mol g}^{-1} \text{h}^{-1}$ ) and CoO ( $11.73 \mu\text{mol g}^{-1} \text{h}^{-1}$ ),

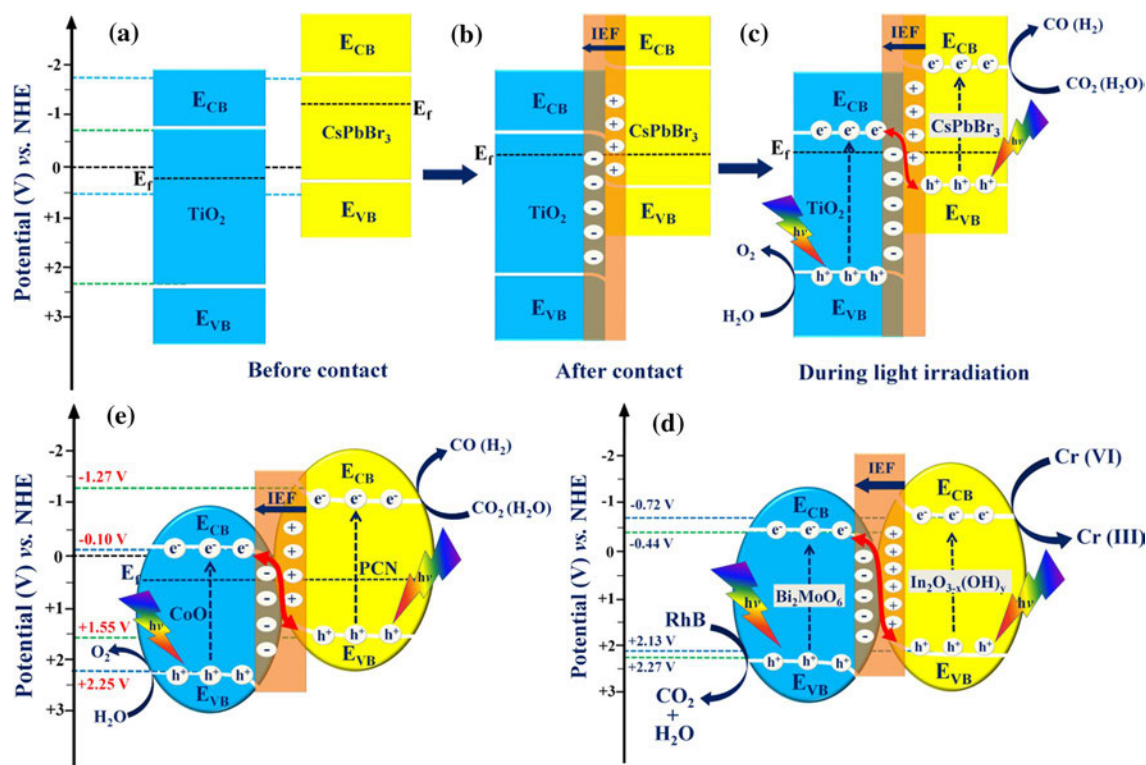


**Fig. 11** **a** Bandgap positions with respective Fermi energy levels ( $E_F$ ) of  $\text{TiO}_2$  and  $\text{CsPbBr}_3$  before contact, **b** redistribution of charge carriers and the generation of the interfacial built-in electric field after intact contact between  $\text{TiO}_2$  and  $\text{CsPbBr}_3$ , and **c** possible S-scheme charge transfer route in  $\text{TiO}_2/\text{CsPbBr}_3$  heterojunction under the exposure of visible light. Adapted with permission (Xu, F. et al. 2020). Copyright 2020, Nature communications. **d** Band diagram showing

rhodamine B (RhB) oxidation (at  $\text{In}_2\text{O}_{3-x}(\text{OH})_y$ ) and Cr (VI) reduction (at  $\text{Bi}_2\text{MoO}_6$ ) over  $\text{In}_2\text{O}_{3-x}(\text{OH})_y/\text{Bi}_2\text{MoO}_6$  S-scheme heterojunction system. Adapted with permission (Li, Zhongfu et al. 2020). Copyright 2020, Elsevier. **e** The band edge potentials and S-scheme charge transfer route followed by CoO coupled with porous polymeric g- $\text{C}_3\text{N}_4$  system for  $\text{CO}_2$  photoreduction. Adapted with permission (Mei et al. 2021). Copyright 2021, Elsevier

respectively (Mei et al. 2021). The porous polymeric g- $\text{C}_3\text{N}_4$  structure fostered the surface adsorption of  $\text{CO}_2$  followed by its reduction through surface-induced charge carriers. After intimate contact, the electrons started migrating from polymeric g- $\text{C}_3\text{N}_4$  to CoO until the Fermi levels are at an equilibrium position which caused the upward and downward band-bending in the case of polymeric g- $\text{C}_3\text{N}_4$  and CoO, respectively. Therefore, under the influence of a built-in-internal electric field, the S-scheme heterojunction smartly consumed relatively unusable photogenerated electrons in the conduction band of CoO and holes in the valence band of polymeric g- $\text{C}_3\text{N}_4$  rendering CoO/ polymeric g- $\text{C}_3\text{N}_4$  heterojunction with higher redox ability beneficial for  $\text{CO}_2$  photoreduction (Fig. 11e). Consequently, with an apt structural arrangement and superior space charge isolation ability retained by S-scheme photocatalytic system, the  $\text{CO}_2$  photoconversion efficacy can be notably enhanced.

## Pollutant degradation

Photocatalytic degradation of organic and inorganic pollutants present in wastewater seems like an effective and economic strategy for environmental protection. Typically, the aqueous phase pollutants can be well decomposed into  $\text{CO}_2$ ,  $\text{H}_2\text{O}$ , and less harmful degraded products mainly by  $\cdot\text{OH}$  and  $\text{O}_2^{\cdot-}$  reactive radicals generated by photocarriers. Therefore, it becomes imperative to reduce the reassembly of photocarriers and boost their spatial isolation for efficient reactive oxygen species production in pollutant degradation (Hasija et al. 2020; Sudhaik et al. 2020b). As reviewed earlier, the S-scheme heterojunction systems with rational regulation of photocarriers and relatively higher redox potential can be efficiently utilized for the photodegradation process.

For instance, Li et al. reported an appealing  $\text{In}_2\text{O}_{3-x}(\text{OH})_y$  coupled  $\text{Bi}_2\text{MoO}_6$  S-scheme heterojunction system designed via a controlled dehydroxylation process of In-based starting materials, used for Cr(VI) reduction and rhodamine B dye



degradation (Li, Zhongfu et al. 2020). The synergy between the S-scheme charge transfer route and residual surface hydroxyl groups remarkably accelerated the surface energy states and modified the interfacial charge migration kinetics. The density of states (DOS) calculated through density functional theory and X-ray photoelectron spectroscopy results were observed to scrutinize the charge carrier distribution and migration direction. The apparent change in the charge carrier density witnessed through X-ray photoelectron spectroscopy, and density functional theory calculations manifested the charge migration that occurred from the conduction band  $\text{Bi}_2\text{MoO}_6$  to the valence band of  $\text{In}_2\text{O}_{3-x}(\text{OH})_y$ . Furthermore, the radical trapping tests performed through electron paramagnetic resonance spectrometer confirmed that the intensity of  $\cdot\text{OH}$  and  $\text{O}_2^{\cdot-}$  radicals was significantly enhanced in  $\text{In}_2\text{O}_{3-x}(\text{OH})_y/\text{Bi}_2\text{MoO}_6$  heterojunction, which was only possible through the construction of the S-scheme.

Based on this, the S-scheme charge transfer pathway followed by  $\text{In}_2\text{O}_{3-x}(\text{OH})_y/\text{Bi}_2\text{MoO}_6$  heterojunction was proposed, as shown in (Fig. 11d). Under the exposure of visible-light, the photogenerated electrons in the conduction band of  $\text{Bi}_2\text{MoO}_6$  recombined with the holes in the valence band of  $\text{In}_2\text{O}_{3-x}(\text{OH})_y$  stimulated by an induced internal electric field. As a result, sufficiently available electrons in the conduction band of  $\text{In}_2\text{O}_{3-x}(\text{OH})_y$  reacted with surface adsorbed  $\text{O}_2$  and generated  $\text{O}_2^{\cdot-}$  radicals. On the other hand, the more accumulated holes in the valence band of  $\text{Bi}_2\text{MoO}_6$  directly participated in the photodegradation reactions. Thus, the  $\text{In}_2\text{O}_{3-x}(\text{OH})_y/\text{Bi}_2\text{MoO}_6$  heterojunction exhibited an enhanced rate of Cr (VI) reduction (96%), and rhodamine B dye oxidation (97.5%) benefitted by S-scheme charge migration kinetics.

A photocatalyst generation of vacancy defects has recently emerged as an appealing tactic to simultaneously modulate the structural and electronic features of photocatalytic material. Inspired by this, Dou et al. engineered oxygen vacancies modified  $\text{Bi}_2\text{O}_3/\text{Bi}_2\text{SiO}_5$  microsphere heterojunctions via a self-assembly one-step solvent assisted route for the photodegradation of methyl orange and colorless phenol (Dou et al. 2020). The presence of oxygen vacancies in the sample was evaluated through low-temperature electron spin resonance and X-ray photoelectron spectroscopy analysis, which showed relatively incremented electron density around the vacancy region. Based on band edge positioning and electron spin resonance results,  $\text{h}^+$ ,  $\cdot\text{OH}$ , and  $\text{O}_2^{\cdot-}$  radicals were the primary species involved in the photodegradation process. The superior generation of reactive radical species was ascribed to the oxygen vacancies, which acted as trapping sites for photocarriers and the S-scheme charge migration route, facilitating the separation of charge carriers in different spatial regions. Consequently, the optimized 1.5% oxygen vacancies- $\text{Bi}_2\text{O}_3/\text{Bi}_2\text{SiO}_5$  showed boosted photocatalytic performance by complete mineralization of

methyl orange and 30% phenol degradation after 60 min exposure under UV–visible light.

Other than aqueous phase pollutants, the potential of photocatalysis has also been exploited to remove  $\text{NO}_x$  from the atmosphere. For instance, Wang et al. constructed dimensionally matched  $\text{Sb}_2\text{WO}_6/\text{BiOBr}$  photocatalyst through precipitation-deposition route at room temperature for  $\text{NO}_x$  oxidation at low concentrations (Wang, Y. et al. 2020). The photocatalytic performance of the optimized 30 wt%  $\text{Sb}_2\text{WO}_6/\text{BiOBr}$  heterojunction was better than that of pristine photocatalysts. According to active species trapping experiments, the S-scheme charge transfer route manifested this increment in the photocatalytic performance of 30 wt%  $\text{Sb}_2\text{WO}_6/\text{BiOBr}$  heterojunction reduces the recombination rate of photocarriers and retain the redox ability for photocatalysis. Furthermore, the S-scheme charge transfer mechanism involved the recombination of relatively useless electrons in the conduction band of  $\text{BiOBr}$  with holes in the valence band of  $\text{Sb}_2\text{WO}_6$  rendering electrons in the conduction band of  $\text{Sb}_2\text{WO}_6$  and holes in the valence band of  $\text{BiOBr}$  with sufficient redox potential for the generation of  $\text{O}_2^{\cdot-}$  and  $\cdot\text{OH}$  radicals, respectively. In a similar work, Ren et al. combined g- $\text{C}_3\text{N}_4$  with  $\text{Sb}_2\text{WO}_6$  via an ultrasound-assisted route and utilized its potential for photocatalytic removal of NO at ppb level (Ren et al. 2021). The report revealed that the 68% NO (continuous flowing) was oxidized under 30 min visible light exposure.

Photocurrent responses and PL spectroscopic results confirmed the effective charge isolation at different spatial regions endowed by S-scheme mode. The optimized 15%- $\text{Sb}_2\text{WO}_6/\text{g-C}_3\text{N}_4$  nanocomposite showed the highest photocurrent density and diminished PL intensity depicting the efficient spatial separation of charge carriers by S-scheme charge migration. The typical mechanism (Fig. 12a-c) involved the redistribution of charge carriers at the interface, which causes upward and downward band-bending in the case of g- $\text{C}_3\text{N}_4$  and  $\text{Sb}_2\text{WO}_6$ , respectively. Thus, under the influence of a built-in-internal electric field, the electrons in the conduction band from  $\text{Sb}_2\text{WO}_6$  recombined with the holes in the valence band of g- $\text{C}_3\text{N}_4$ , leaving behind electrons and holes with relatively higher potential to participate in photocatalytic reactions. Summarily, via constructing S-scheme heterostructures, the charge separation kinetics can be significantly improved resulted in the enhanced generation of reactive radical species responsible for the degradation of pollutants.

## Bacterial inactivation

Traditional water disinfection processes involving chlorination, ozonation, and UV disinfection are not viable due to the generation of secondary by-products and exceptional energy-consuming behavior. In this context, ‘photocatalytic

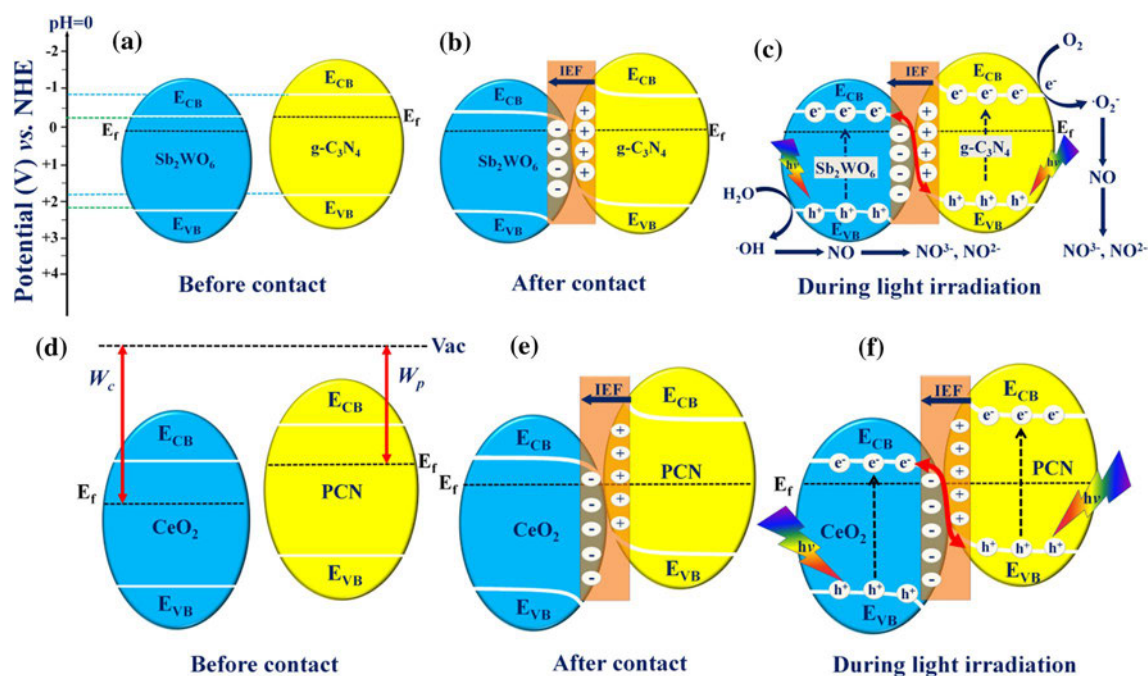


**Fig. 12** Band edge positioning and Fermi level alignment ( $E_f$ ) of  $\text{Sb}_2\text{WO}_6$  and  $\text{g-C}_3\text{N}_4$  before contact **a**, redistribution of charges and the subsequent generation of an internal electric field at the interface of  $\text{Sb}_2\text{WO}_6$  and  $\text{g-C}_3\text{N}_4$  **b**, and possible S-scheme charge transfer route followed by  $\text{Sb}_2\text{WO}_6/\text{g-C}_3\text{N}_4$  nanocomposite for the decomposition of  $\text{NO}$  facilitated by reactive radical species **c**. Adapted with per-

mission (Ren et al. 2021). Copyright 2021, Elsevier. Diagrammatic representation of: d difference in the work function of  $\text{CeO}_2$  ( $W_c$ ) and polymeric  $\text{g-C}_3\text{N}_4$  ( $W_p$ ) before contact, e induced internal electric field after contact, and f S-scheme charge transfer mode in 0D/2D  $\text{CeO}_2/\text{g-C}_3\text{N}_4$  heterojunction under visible light irradiation. Adapted with permission (Xia, P. et al. 2020). Copyright 2019, Wiley

disinfection process' concerning the generation of dominant reactive species like  $\text{O}_2^{\cdot-}$  and  $\cdot\text{OH}$  radicals by excitation of semiconductor catalysts are limelight to its cost-effectiveness and environment-friendly nature. Notably, a photocatalytic system with suitable redox potentials to generate  $\text{O}_2^{\cdot-}$  and  $\cdot\text{OH}$  radicals as major species is promising for photocatalytic biohazard disinfection (Wang et al. 2017). So far, the S-scheme photocatalytic systems with fascinating space charge isolation ability can substantially inactivate bacteria through reserved photocarriers with strong potentials.

To support this concept, Xia et al. designed 0D/2D  $\text{CeO}_2/\text{S-scheme}$  heterojunction via in situ wet chemistry followed by thermal treatment and utilized it for *Staphylococcus Aureus* inactivation (Xia, P. et al. 2020). The report further revealed that the 0D/2D  $\text{CeO}_2/\text{polymeric g-C}_3\text{N}_4$  heterojunction exhibited a remarkable photocatalytic inactivation rate of *Staphylococcus Aureus* (88.1%) under the exposure of visible light, which was 8.2 and 2.7 times superior to polymeric  $\text{g-C}_3\text{N}_4$  (10.7%) and  $\text{CeO}_2$  (32.2%), respectively. The increment in photocatalytic efficacy was due to the effective charge separation at distinct spatial regions and high redox ability to generate reactive species provided by S-scheme charge transfer mode facilely (Fig. 12d-f). The computational studies involving 3D charge density difference and planar-averaged electron density difference validated the

phenomenon of band-bending after coupling  $\text{CeO}_2$  possessing lower Fermi energy levels with polymeric  $\text{g-C}_3\text{N}_4$ .

Furthermore, the S-scheme charge transfer route was verified with the in situ irradiated X-ray photoelectron spectroscopy analysis. The X-ray photoelectron spectroscopy spectra of C and N exhibited a substantial shift from higher binding energy in darkness to lower binding energy under irradiation. Besides, in the case of Ce, the binding energy increased under illumination, suggesting the role of Ce as an electron donor. Thus, through X-ray photoelectron spectroscopy results, migration of photoexcited electrons from the conduction band of  $\text{CeO}_2$  to the valence band of polymeric  $\text{g-C}_3\text{N}_4$  was observed, which helped to attain the high redox ability beneficial for the generation of dominant  $\text{O}_2^{\cdot-}$  and  $\cdot\text{OH}$  radicals responsible for *S. aureus* sterilization.

In another work,  $\text{g-C}_3\text{N}_4/\text{Ag}_2\text{WO}_4$  S-scheme heterojunction was coated by fluorocarbon resin coating, which exhibited excellent bacteriostatic ability against *Escherichia coli* (*E.coli*) in sterile seawater with stability up to 3 consecutive cycles under visible light illumination (Zhu et al. 2020). This was attributed to the inherent Ag ions property for bacterial disinfection, hydrophobic nature of fluorocarbon resin coating, and adequately due to the S-scheme charge transfer route. The radical trapping experiment confirmed the formation of  $\text{O}_2^{\cdot-}$  and  $\cdot\text{OH}$  radicals (which majorly participated in

**Table 1** S-scheme photocatalytic systems for various applications

Photocatalyst	Charge transfer mode	Characterization	Mechanism	Targeted application	Photocatalytic efficacy	Apparent quantum yield/efficiency	Refs
$\text{WO}_3/\text{CdIn}_2\text{S}_4$	S-scheme	X-ray photoelectron and electron spin resonance spectroscopy	Tight interfacial contact and enhanced isolation and migration of photocarriers	Tetracycline hydrochloride degradation	Tetracycline hydrochloride degradation = 72.0%	–	Pei et al. (2021)
$\text{BiOBr}/\text{BiO}(\text{HCOO})\text{Br-x}$	S-scheme	X-ray photoelectron and electron spin resonance spectroscopy	Intact interface junction and rapid migration of photocarriers	Malachite green, rhodamine B and tetracycline degradation	Malachite green degradation = 60% Rhodamine B degradation = 98% Tetracycline degradation = 80%	–	Li et al. (2020)
$\text{In}_2\text{S}_3/\text{Bi}_2\text{O}_3\text{CO}_3$	S-scheme	X-ray photoelectron and electron spin resonance spectroscopy	Reductive photocatalytic system with enhancement in light utilization region and suppressed recombination of photocarriers	Rhodamine B and tetracycline degradation	Rhodamine B degradation = 91% Tetracycline degradation = 70%	–	Fan et al. (2020)
$\text{LaNiO}_3/\text{TiO}_2$	S-scheme	X-ray photoelectron spectroscopy and spin trapping experiment	Reduced charge recombination and enhanced migration	Methyl orange degradation	Methyl orange degradation = 57.6%	–	Chen et al. (2020)
$\text{BiVO}_4/\text{Ag}_3\text{VO}_4$	S-scheme	X-ray photoelectron spectroscopy	Inhibited charge carrier reassembly with enhanced lifetime	Methylene blue	Methylene blue degradation = 93.48%	–	Liu et al. (2021)
$\text{Cd}_{0.5}\text{Zn}_{0.5}\text{S}/\text{g-C}_3\text{N}_4$	S-scheme	X-ray photoelectron and electron spin resonance spectroscopy	abundant reactivity sites and excellent separation/transfer efficiency of charge carriers on the surface and at the interface	Rhodamine B degradation	Rhodamine B degradation rate constant = 0.0817 min <sup>-1</sup>	–	Qin et al. (2020b)
$\text{ZnO}/\text{CdSe}$ -diethylenetriamine with Pt co-catalyst	S-scheme	X-ray photoelectron spectroscopy	(1) Effective charge isolation and migration through S-scheme and Pt co-catalyst (2) Enhanced optical absorption due to surface plasmon resonance effect induced by Pt-loading	$\text{H}_2$ production	$\text{H}_2$ production = 11.09 mol g <sup>-1</sup> h <sup>-1</sup>	–	Li et al. (2020)

**Table 1** (continued)

Photocatalyst	Charge transfer mode	Characterization	Mechanism	Targeted application	Photocatalytic efficacy	Apparent quantum yield/efficiency	Refs
g-C <sub>3</sub> N <sub>4</sub> /Zn <sub>0.2</sub> Cd <sub>0.8</sub> S-DETA WO <sub>3</sub> /TiO <sub>2</sub> /rGO	S-scheme	X-ray photoelectron spectroscopy	Efficient charge isolation and migration	H <sub>2</sub> production	H <sub>2</sub> production = 6.69 mmol g <sup>-1</sup> h <sup>-1</sup>	17.8%	Mei et al. (2020)
	S-scheme	X-ray photoelectron and electron spin resonance spectroscopy	(1) Enhanced light absorption (2) Reduced reassembly of photocarriers (3) Increased active sites at the surface of photocatalyst	H <sub>2</sub> production	H <sub>2</sub> production = 245.8 μmol g <sup>-1</sup> h <sup>-1</sup>	1.4% at 365 nm	He et al. (2020)
Zn <sub>0.5</sub> Cd <sub>0.5</sub> S/WO <sub>3</sub>	S-scheme	X-ray photoelectron spectroscopy	(1) Good electrical conductivity (2) Improved optical absorption in visible light region	H <sub>2</sub> production	H <sub>2</sub> production = 819.54 μmol	6.19% at 400 nm	Gong et al. (2019)
CuI-graphdiyne/g-C <sub>3</sub> N <sub>4</sub>	S-scheme	X-ray photoelectron spectroscopy	(1) Prolonged lifetime of charge carriers (2) enhanced electron density (3) reduced overpotential for H <sub>2</sub> production	H <sub>2</sub> production	H <sub>2</sub> production = 8.9 × pure g-C <sub>3</sub> N <sub>4</sub>	–	Jin et al. (2020)

the inactivation process) by reducing molecular  $O_2$  and oxidation of  $OH^-$  at the conduction band of g- $C_3N_4$  and valence band of  $Ag_2WO_4$ , respectively. As a whole, the construction of S-scheme photocatalysts with suitable bandgap positioning can generate highly reactive radical species owing to the spatial distribution of oxidation sites and reduction sites exceedingly desirable for the photocatalytic bacterial inactivation process. Table 1 summarizes various S-scheme photocatalysts for different photocatalytic systems.

## Conclusion

Extensive research has been devoted to the progress of various photocatalytic systems. Studies to date have shown that single component photocatalysts are unlikely to attain adequate efficiency and stability for practical applications. Thus, multicomponent heterojunctions have been explored to enhance the light absorption ability, improve charge separation, and increase the lifetime of charge carriers. The present review describes the proposition of novel S-scheme photocatalysts with their potential in various photocatalytic realms. It is conspicuous that the S-scheme heterojunctions simultaneously acquire high redox ability and broaden solar energy utilization, thereby overcoming the inherent drawbacks of traditional type-II and Z-scheme photocatalytic systems.

The S-scheme charge transfer route is benefited from the band edge bending, internal electric field, and Coulombic interactions between opposite charges. These stepwise consequences are the key to eliminate the lower redox potential photogenerated electrons and holes while preserving the effective ones. We anticipate that the theoretical simulations and in/ex situ experiments provide an in-depth understanding of the unique S-scheme mechanism. Precisely, the shift in binding energies in the X-ray photoelectron spectroscopy spectrum after forming the heterojunction, radical trapping tests through electron paramagnetic resonance studies, and the intact interfacial contact verified through atomic force microscopy analysis validate the S-scheme heterojunctions.

However, the existing challenges of a thermodynamic barrier, Fermi level adjustment, and optimized contact surface area between oxidative and reductive photocatalysts are critical. Therefore, development in modifying S-scheme heterojunctions requires profound exploration in the following directions. Firstly, the deposition of co-catalysts onto the respective oxidation and reduction sites enhances the electron-hole pair separation rate and lowers the activation barrier for the photocatalytic mechanism. Secondly, the incorporation of dopants tends to widen the Fermi level gap for its feasible alignment and alters the electronic structure to obtain extended solar energy absorption. Finally, the interfacial contact in the S-scheme photocatalysts is rationally

controlled by constructing two-dimensional face-to-face heterojunctions to enlarge the space charge region, which serves as a charge recombination center.

Currently, the development of S-scheme photocatalysts is still at an early stage. The applications of S-scheme photocatalysts are limited mainly due to their usage as powder photocatalysts and the suitable approach involving the selection of adjoining n-type semiconductors. Thus, it is highly desirable to expand the area of pioneering S-scheme heterostructures to attain environmental and energy-related photocatalytic concerns sustainably.

**Acknowledgements** The corresponding author, Dr. Pankaj Raizada is thankful to H.P. Council for Science, Technology & Environment (HIMCOSTE), Himachal Pradesh, for financial support through research project no. HIMCOSTE (R&D)/2019-20-2.5(4).

## References

- Bagheri S, TermehYousefi A, Do T-O (2017) Photocatalytic pathway toward degradation of environmental pharmaceutical pollutants: structure, kinetics and mechanism approach. *Catal Sci Technol* 7(20):4548–4569. <https://doi.org/10.1039/C7CY00468K>
- Bai S, Jiang J, Zhang Q, Xiong Y (2015) Steering charge kinetics in photocatalysis: intersection of materials syntheses, characterization techniques and theoretical simulations. *Chem Soc Rev* 44(10):2893–2939. <https://doi.org/10.1039/C5CS00064E>
- Bai S, Wang X, Hu C, Xie M, Jiang J, Xiong Y (2014) Two-dimensional g- $C_3N_4$ : an ideal platform for examining facet selectivity of metal co-catalysts in photocatalysis. *Chem Commun* 50(46):6094–6097. <https://doi.org/10.1039/C4CC00745J>
- Banerjee S, Pillai SC, Falaras P, O'Shea KE, Byrne JA, Dionysiou DD (2014) New Insights into the Mechanism of Visible Light Photocatalysis. *J Phys Chem Lett* 5(15):2543–2554. <https://doi.org/10.1021/jz501030x>
- Cerrato E, Paganini MC (2020) Mechanism of visible photon absorption: unveiling of the  $C_3N_4$ -ZnO photoactive interface by means of EPR spectroscopy. *Mater Adv* 1(7):2357–2367. <https://doi.org/10.1039/D0MA00451K>
- Chen B-R, Nguyen V-H, Wu JCS, Martin R, Kočí K (2016) Production of renewable fuels by the photohydrogenation of  $CO_2$ : effect of the Cu species loaded onto  $TiO_2$  photocatalysts. *Phys Chem Chem Phys* 18(6):4942–4951. <https://doi.org/10.1039/C5CP06999H>
- Chen C, Zhou J, Geng J, Bao R, Wang Z, Xia J, Li HJASS (2020a) Perovskite  $LaNiO_3/TiO_2$  step-scheme heterojunction with enhanced photocatalytic activity. *Appl Surf Sci* 503:144287. <https://doi.org/10.1016/j.apsusc.2019.144287>
- Chen J, Liu T, Zhang H, Wang B, Zheng W, Wang X, Li J, Zhong J (2020b) One-pot preparation of double S-scheme  $Bi_2S_3/MoO_3/C_3N_4$  heterojunctions with enhanced photocatalytic activity originated from the effective charge pairs partition and migration. *Appl Surf Sci* 527:146788. <https://doi.org/10.1016/j.apsusc.2020.146788>
- Chen Y, Su F, Xie H, Wang R, Ding C, Huang J, Xu Y, Ye L (2021) One-step construction of S-scheme heterojunctions of N-doped  $MoS_2$  and S-doped g- $C_3N_4$  for enhanced photocatalytic hydrogen evolution. *Chem Eng J* 404:126498. <https://doi.org/10.1016/j.cej.2020.126498>



- Cheng Y-H, Nguyen V-H, Chan H-Y, Wu JCS, Wang W-H (2015) Photo-enhanced hydrogenation of CO<sub>2</sub> to mimic photosynthesis by CO co-feed in a novel twin reactor. *Appl Energy* 147:318–324. <https://doi.org/10.1016/j.apenergy.2015.02.085>
- Dai B, Chen Y, Hao S-M, Huang H, Kou J, Lu C, Lin Z, Xu Z (2020) Sustainable internal electric field for enhanced photocatalysis: from material design to energy utilization. *J Phys Chem Lett* 11(17):7407–7416. <https://doi.org/10.1021/acs.jpclett.0c00889>
- Deng H, Fei X, Yang Y, Fan J, Yu J, Cheng B, Zhang L (2021) S-scheme heterojunction based on p-type ZnMn<sub>2</sub>O<sub>4</sub> and n-type ZnO with improved photocatalytic CO<sub>2</sub> reduction activity. *Chem Eng J* 409:127377. <https://doi.org/10.1016/j.cej.2020.127377>
- Di T, Xu Q, Ho W, Tang H, Xiang Q, Yu J (2019) Review on Metal Sulphide-based Z-scheme photocatalysts. *ChemCatChem* 11(5):1394–1411. <https://doi.org/10.1002/cctc.201802024>
- Dou L, Jin X, Chen J, Zhong J, Li J, Zeng Y, Duan R (2020) One-pot solvothermal fabrication of S-scheme OV<sub>s</sub>-Bi<sub>2</sub>O<sub>3</sub>/Bi<sub>2</sub>SiO<sub>5</sub> microsphere heterojunctions with enhanced photocatalytic performance toward decontamination of organic pollutants. *Appl Surf Sci* 527:146775. <https://doi.org/10.1016/j.apsusc.2020.146775>
- Fan H, Zhou H, Li W, Gu S, Zhou G (2020) Facile fabrication of 2D/2D step-scheme In<sub>2</sub>S<sub>3</sub>/Bi<sub>2</sub>O<sub>2</sub>CO<sub>3</sub> heterojunction towards enhanced photocatalytic activity. *Appl Surf Sci* 504:144351. <https://doi.org/10.1016/j.apsusc.2019.144351>
- Fox MA, Dulay MT (1993) Heterogeneous photocatalysis. *Chem Rev* 93(1):341–357. <https://doi.org/10.1021/cr00017a016>
- Fu J, Xu Q, Low J, Jiang C, Yu J (2019) Ultrathin 2D/2D WO<sub>3</sub>/g-C<sub>3</sub>N<sub>4</sub> step-scheme H<sub>2</sub>-production photocatalyst. *Appl Catal B* 243:556–565. <https://doi.org/10.1016/j.apcatb.2018.11.011>
- Fujishima A, Honda K (1972) Electrochemical photolysis of water at a semiconductor electrode. *Nature* 238(5358):37–38. <https://doi.org/10.1038/238037a0>
- Gao C, Wang J, Xu H, Xiong Y (2017) Coordination chemistry in the design of heterogeneous photocatalysts. *Chem Soc Rev* 46(10):2799–2823. <https://doi.org/10.1039/C6CS00727A>
- Ge H, Xu F, Cheng B, Yu J, Ho W (2019) S-Scheme Heterojunction TiO<sub>2</sub>/CdS Nanocomposite Nanofiber as H<sub>2</sub>-Production Photocatalyst. *ChemCatChem* 11(24):6301–6309. <https://doi.org/10.1002/cctc.201901486>
- Gong H, Hao X, Jin Z, Ma Q (2019) WP modified S-scheme Zn 0.5 Cd 0.5 S/WO<sub>3</sub> for efficient photocatalytic hydrogen production. *New J. Chem.* 43(48):19159–19171. <https://doi.org/10.1039/C9NJ04584H>
- Hasija V, Raizada P, Hosseini-Bandegharai A, Singh P, Nguyen V-H (2020) Synthesis and photocatalytic activity of Ni–Fe Layered double hydroxide modified sulphur doped graphitic carbon nitride (SGCN/Ni–Fe LDH) photocatalyst for 2,4-dinitrophenol degradation. *Top Catal* 63(11):1030–1045. <https://doi.org/10.1007/s11244-020-01359-z>
- Hasija V, Raizada P, Sudhaik A, Sharma K, Kumar A, Singh P, Jonnalagadda SB, Thakur VK (2019) Recent advances in noble metal free doped graphitic carbon nitride based nanohybrids for photocatalysis of organic contaminants in water: a review. *Appl Mater Today* 15:494–524. <https://doi.org/10.1016/j.apmt.2019.04.003>
- He F, Meng A, Cheng B, Ho W, Yu J (2020) Enhanced photocatalytic H<sub>2</sub>-production activity of WO<sub>3</sub>/TiO<sub>2</sub> step-scheme heterojunction by graphene modification. *Chinese J Catal* 41(1):9–20. [https://doi.org/10.1016/S1872-2067\(19\)63382-6](https://doi.org/10.1016/S1872-2067(19)63382-6)
- Hu T, Dai K, Zhang J, Chen S (2020a) Noble-metal-free Ni<sub>2</sub>P modified step-scheme SnNb<sub>2</sub>O<sub>6</sub>/CdS-diethylenetriamine for photocatalytic hydrogen production under broadband light irradiation. *Appl Catal B* 269:118844. <https://doi.org/10.1016/j.apcatb.2020.118844>
- Hu X, Wang G, Wang J, Hu Z, Su Y (2020b) Step-scheme NiO/BiOI heterojunction photocatalyst for rhodamine photodegradation. *Appl Surf Sci* 511:145499. <https://doi.org/10.1016/j.apsusc.2020.145499>
- Huang C-W, Nguyen B-S, Wu JCS, Nguyen V-H (2020) A current perspective for photocatalysis towards the hydrogen production from biomass-derived organic substances and water. *Int J Hydrog Energy* 45(36):18144–18159. <https://doi.org/10.1016/j.ijhydene.2019.08.121>
- Huang D, Chen S, Zeng G, Gong X, Zhou C, Cheng M, Xue W, Yan X, Li J (2019) Artificial Z-scheme photocatalytic system: what have been done and where to go? *Coord Chem Rev* 385:44–80. <https://doi.org/10.1016/j.ccr.2018.12.013>
- Huo Y, Zhang J, Wang Z, Dai K, Pan C, Liang C (2021) Efficient interfacial charge transfer of 2D/2D porous carbon nitride/bismuth oxychloride step-scheme heterojunction for boosted solar-driven CO<sub>2</sub> reduction. *J Colloid Interface Sci* 585:684–693. <https://doi.org/10.1016/j.jcis.2020.10.048>
- Jiang L, Yuan X, Pan Y, Liang J, Zeng G, Wu Z, Wang H (2017) Doping of graphitic carbon nitride for photocatalysis: a review. *Appl Catal B* 217:388–406. <https://doi.org/10.1016/j.apcatb.2017.06.003>
- Jiang L, Yuan X, Zeng G, Liang J, Wu Z, Wang H (2018) Construction of an all-solid-state Z-scheme photocatalyst based on graphite carbon nitride and its enhancement to catalytic activity. *Environ Sci Nano* 5(3):599–615. <https://doi.org/10.1039/C7EN01031A>
- Jin Z, Zhang L, Wang G, Li Y, Wang Y (2020) Graphdiyne formed a novel CuI-GD/gC<sub>3</sub>N<sub>4</sub> S-scheme heterojunction composite for efficient photocatalytic hydrogen evolution. *Sustain Energy Fuels* 4(10):5088–5101. <https://doi.org/10.1039/D0SE01011A>
- Kalyanasundaram K. 2013 Photochemical applications of solar energy: photocatalysis and photodecomposition of water, *Photochemistry: The Royal Society of Chemistry*. <https://doi.org/10.1039/9781849737722-00182>
- Kanakaraju D, Glass BD, Oelgemöller M (2014) Titanium dioxide photocatalysis for pharmaceutical wastewater treatment. *Environ Chem Lett* 12(1):27–47. <https://doi.org/10.1007/s10311-013-0428-0>
- Kumar A, Raizada P, Hosseini-Bandegharai A, Thakur VK, Nguyen V-H, Singh P (2021a) C-, N-Vacancy defect engineered polymeric carbon nitride towards photocatalysis: viewpoints and challenges. *J Mater Chem A* 9(1):111–153. <https://doi.org/10.1039/D0TA08384D>
- Kumar A, Raizada P, Kumar Thakur V, Saini V, Khan AP, A., Singh, N., Singh, P., (2021b) An overview on polymeric carbon nitride assisted photocatalytic CO<sub>2</sub> reduction: Strategically manoeuvring solar to fuel conversion efficiency. *Chem Eng Sci* 230:116219. <https://doi.org/10.1016/j.ces.2020.116219>
- Kumar A, Raizada P, Singh P, Hosseini-Bandegharai A, Thakur VK (2020) Facile synthesis and extended visible light activity of oxygen and sulphur co-doped carbon nitride quantum dots modified Bi<sub>2</sub>MoO<sub>6</sub> for phenol degradation. *J Photochem Photobiol A* 397:112588. <https://doi.org/10.1016/j.jphotochem.2020.112588>
- Li D, Yu JC-C, Nguyen V-H, Wu JCS, Wang X (2018) A dual-function photocatalytic system for simultaneous separating hydrogen from water splitting and photocatalytic degradation of phenol in a twin-reactor. *Appl Catal B* 239:268–279. <https://doi.org/10.1016/j.apcatb.2018.08.010>
- Li H, Tu W, Zhou Y, Zou Z (2016) Z-Scheme photocatalytic systems for promoting photocatalytic performance: recent progress and future challenges. *Adv Sci* 3(11):1500389. <https://doi.org/10.1002/adv.201500389>
- Li S, Han Q, Jia X, Zahid AH, Bi H (2020a) Room-temperature one-step synthesis of tube-like S-scheme BiOBr/BiO (HCOO) Br-x heterojunction with excellent visible-light photocatalytic

- performance. *Appl Surf Sci* 530:147208. <https://doi.org/10.1016/j.apsusc.2020.147208>
- Li X, Xiong J, Gao X, Ma J, Chen Z, Kang B, Liu J, Li H, Feng Z, Huang J (2020b) Novel BP/BiOBr S-scheme nano-heterojunction for enhanced visible-light photocatalytic tetracycline removal and oxygen evolution activity. *J Hazard Mater* 387:121690. <https://doi.org/10.1016/j.jhazmat.2019.121690>
- Li X, Yu J, Jaroniec M, Chen X (2019) Cocatalysts for selective Photoreduction of CO<sub>2</sub> into solar fuels. *Chem Rev* 119(6):3962–4179. <https://doi.org/10.1021/acs.chemrev.8b00400>
- Li Z, Jin D, Wang Z (2020c) ZnO/CdSe-diethylenetriamine nanocomposite as a step-scheme photocatalyst for photocatalytic hydrogen evolution. *Appl Surf Sci* 529:147071. <https://doi.org/10.1016/j.apsusc.2020.147071>
- Li Z, Wu Z, He R, Wan L, Zhang S (2020d) In<sub>2</sub>O<sub>3</sub>-x(OH)y/Bi<sub>2</sub>MoO<sub>6</sub> S-scheme heterojunction for enhanced photocatalytic performance. *J Mater Sci Technol* 56:151–161. <https://doi.org/10.1016/j.jmst.2020.02.061>
- Liras M, Barawi M, de la Peña O'Shea VA (2019) Hybrid materials based on conjugated polymers and inorganic semiconductors as photocatalysts: from environmental to energy applications. *Chem Soc Rev* 48(22):5454–5487. <https://doi.org/10.1039/C9CS00377K>
- Liu L, Hu T, Dai K, Zhang J, Liang C (2021) A novel step-scheme BiVO<sub>4</sub>/Ag<sub>3</sub>VO<sub>4</sub> photocatalyst for enhanced photocatalytic degradation activity under visible light irradiation. *Chinese J Catal* 42(1):46–55. [https://doi.org/10.1016/S1872-2067\(20\)63560-4](https://doi.org/10.1016/S1872-2067(20)63560-4)
- Liu Y, Gong Z, Lv H, Ren H, Xing X (2020) Rational design of Au decorated Mn<sub>0.5</sub>Cd<sub>0.5</sub>/WO<sub>3</sub> step-scheme heterostructure with multichannel charge transfer and efficient H<sub>2</sub> generation. *Appl. Surf. Sci.* 526:146734. <https://doi.org/10.1016/j.apsusc.2020.146734>
- Low J, Jiang C, Cheng B, Wageh S, Al-Ghamdi AA, Yu J (2017a) A review of direct z-scheme photocatalysts. *Small Methods* 1(5):1700080. <https://doi.org/10.1002/smt.201700080>
- Low J, Yu J, Jaroniec M, Wageh S, Al-Ghamdi AA (2017b) Heterojunction photocatalysts. *Adv Mater* 29(20):1601694. <https://doi.org/10.1002/adma.201601694>
- Mao J, Peng T, Zhang X, Li K, Ye L, Zan L (2013) Effect of graphitic carbon nitride microstructures on the activity and selectivity of photocatalytic CO<sub>2</sub> reduction under visible light. *Catal Sci Technol* 3(5):1253–1260. <https://doi.org/10.1039/C3CY20822B>
- Mecha AC, Chollom MN (2020) Photocatalytic ozonation of wastewater: a review. *Environ Chem Lett* 18(5):1491–1507. <https://doi.org/10.1007/s10311-020-01020-x>
- Mei F, Li Z, Dai K, Zhang J, Liang C, C.J.C.J.o.C. (2020) Step-scheme porous g-C<sub>3</sub>N<sub>4</sub>/ZnO 2Cd0 8S-DETA composites for efficient and stable photocatalytic H<sub>2</sub> production. *Chinese J. Catal.* 41(1):41–49. [https://doi.org/10.1016/S1872-2067\(19\)63389-9](https://doi.org/10.1016/S1872-2067(19)63389-9)
- Mei F, Zhang J, Liang C, Dai K (2021) Fabrication of novel CoO/porous graphitic carbon nitride S-scheme heterojunction for efficient CO<sub>2</sub> photoreduction. *Mater Lett* 282:128722. <https://doi.org/10.1016/j.matlet.2020.128722>
- Mousset E, Dionysiou DD (2020) Photoelectrochemical reactors for treatment of water and wastewater: a review. *Environ Chem Lett* 18(4):1301–1318. <https://doi.org/10.1007/s10311-020-01014-9>
- Natarajan TS, Thampi KR, Tayade RJ (2018) Visible light driven redox-mediator-free dual semiconductor photocatalytic systems for pollutant degradation and the ambiguity in applying Z-scheme concept. *Appl Catal B* 227:296–311. <https://doi.org/10.1016/j.apcatb.2018.01.015>
- Nguyen TD, Nguyen V-H, Nanda S, Vo D-VN, Nguyen VH, Van Tran T, Nong LX, Nguyen TT, Bach L-G, Abdullah B, Hong S-S, Van Nguyen T (2020a) BiVO<sub>4</sub> photocatalysis design and applications to oxygen production and degradation of organic compounds: a review. *Environ Chem Lett* 18(6):1779–1801. <https://doi.org/10.1007/s10311-020-01039-0>
- Nguyen TP, Nguyen DLT, Nguyen V-H, Le T-H, Vo D-VN, Trinh QT, Bae S-R, Chae SY, Kim SY, Le QV (2020b) Recent advances in TiO<sub>2</sub>-based photocatalysts for reduction of CO<sub>2</sub> to fuels. *Nano-materials* 10(2):337
- Nguyen V-H, Chan H-Y, Wu JCS, Bai H (2012) Direct gas-phase photocatalytic epoxidation of propylene with molecular oxygen by photocatalysts. *Chem Eng J* 179:285–294. <https://doi.org/10.1016/j.cej.2011.11.003>
- Nguyen V-H, Lin SD, Wu JC-S (2015) Synergetic photo-epoxidation of propylene over VTi/MCM-41 mesoporous photocatalysts. *J Catal* 331:217–227. <https://doi.org/10.1016/j.jcat.2015.09.001>
- Nguyen V-H, Nguyen B-S, Jin Z, Shokouhimehr M, Jang HW, Hu C, Singh P, Raizada P, Peng W, Shiung Lam S, Xia C, Nguyen CC, Kim SY, Le QV (2020c) Towards artificial photosynthesis: Sustainable hydrogen utilization for photocatalytic reduction of CO<sub>2</sub> to high-value renewable fuels. *Chem Eng J* 402:126184. <https://doi.org/10.1016/j.cej.2020.126184>
- Nguyen V-H, Nguyen B-S, Vo H-T, Nguyen CC, Bae S-R, Kim SY, Le QV (2020d) Recent advances in selective photo-epoxidation of propylene: a review. *Catalysts* 10(1):87. <https://doi.org/10.3390/catal10010087>
- Nguyen V-H, Phan Thi L-A, Van Le Q, Singh P, Raizada P, Kajitvichyanukul P (2020e) Tailored photocatalysts and revealed reaction pathways for photodegradation of polycyclic aromatic hydrocarbons (PAHs) in water, soil and other sources. *Chemosphere* 260:127529. <https://doi.org/10.1016/j.chemosphere.2020.127529>
- Nguyen V-H, Smith SM, Wantala K, Kajitvichyanukul P (2020f) Photocatalytic remediation of persistent organic pollutants (POPs): a review. *Arabian J Chem* 13(11):8309–8337. <https://doi.org/10.1016/j.arabj.2020.04.028>
- Nguyen V-H, Wu JCS (2018) Recent developments in the design of photoreactors for solar energy conversion from water splitting and CO<sub>2</sub> reduction. *Appl Catal A* 550:122–141. <https://doi.org/10.1016/j.apcata.2017.11.002>
- Ohtani B (2010) Photocatalysis A to Z—what we know and what we do not know in a scientific sense. *J Photochem Photobiol C* 11(4):157–178. <https://doi.org/10.1016/j.jphotochemrev.2011.02.001>
- Ohtani B (2014) Revisiting the fundamental physical chemistry in heterogeneous photocatalysis: its thermodynamics and kinetics. *Phys Chem Chem Phys* 16(5):1788–1797. <https://doi.org/10.1039/C3CP53653J>
- Patnaik S, Sahoo DP, Parida K (2021) Recent advances in anion doped g-C<sub>3</sub>N<sub>4</sub> photocatalysts: a review. *Carbon* 172:682–711. <https://doi.org/10.1016/j.carbon.2020.10.073>
- Pei C-Y, Chen Y-G, Wang L, Chen W, Huang G-B (2021) Step-scheme WO<sub>3</sub>/CdIn<sub>2</sub>S<sub>4</sub> hybrid system with high visible light activity for tetracycline hydrochloride photodegradation. *Appl Surf Sci* 535:147682. <https://doi.org/10.1016/j.apsusc.2020.147682>
- Peng J, Shen J, Yu X, Tang H, Zulfiqar L, Q. (2021) Construction of LSPR-enhanced 0D/2D CdS/MoO<sub>3</sub>-x S-scheme heterojunctions for visible-light-driven photocatalytic H<sub>2</sub> evolution. *Chinese J Catal* 42(1):87–96. [https://doi.org/10.1016/S1872-2067\(20\)63595-1](https://doi.org/10.1016/S1872-2067(20)63595-1)
- Qin D, Xia Y, Li Q, Yang C, Qin Y, Lv K (2020a) One-pot calcination synthesis of Cd<sub>0.5</sub>Zn<sub>0.5</sub>/g-C<sub>3</sub>N<sub>4</sub> photocatalyst with a step-scheme heterojunction structure. *J Mater Sci Technol* 56:206–215. <https://doi.org/10.1016/j.jmst.2020.03.034>
- Qin D, Xia Y, Li Q, Yang C, Qin Y, Lv K (2020b) One-pot calcination synthesis of Cd<sub>0.5</sub>Zn<sub>0.5</sub>/g-C<sub>3</sub>N<sub>4</sub> photocatalyst with a step-scheme heterojunction structure. *J Mater Sci Technol.* <https://doi.org/10.1016/j.jmst.2020.03.034>
- Qin Y, Li H, Lu J, Feng Y, Meng F, Ma C, Yan Y, Meng M (2020c) Synergy between van der waals heterojunction and vacancy in

- ZnIn<sub>2</sub>S<sub>4</sub>/g-C<sub>3</sub>N<sub>4</sub> 2D/2D photocatalysts for enhanced photocatalytic hydrogen evolution. *Appl Catal B* 277:119254. <https://doi.org/10.1016/j.apcatb.2020.119254>
- Raizada P, Kumar A, Hasija V, Singh P, Thakur VK, Khan AAP (2021) An overview of converting reductive photocatalyst into all solid-state and direct Z-scheme system for water splitting and CO<sub>2</sub> reduction. *J Ind Eng Chem* 93:1–27. <https://doi.org/10.1016/j.jiec.2020.09.006>
- Ren Y, Li Y, Wu X, Wang J, Zhang G (2021) S-scheme Sb<sub>2</sub>WO<sub>6</sub>/g-C<sub>3</sub>N<sub>4</sub> photocatalysts with enhanced visible-light-induced photocatalytic NO oxidation performance. *Chinese J Catal* 42(1):69–77. [https://doi.org/10.1016/S1872-2067\(20\)63631-2](https://doi.org/10.1016/S1872-2067(20)63631-2)
- Rongan H, Haijuan L, Huimin L, Difa X, Liuyang Z (2020) S-scheme photocatalyst Bi<sub>2</sub>O<sub>3</sub>/TiO<sub>2</sub> nanofiber with improved photocatalytic performance. *J Mater Sci Technol* 52:145–151. <https://doi.org/10.1016/j.jmst.2020.03.027>
- Sakthivel T, Venugopal G, Durairaj A, Vasanthkumar S, Huang X (2019) Utilization of the internal electric field in semiconductor photocatalysis: a short review. *J Ind Eng Chem* 72:18–30. <https://doi.org/10.1016/j.jiec.2018.12.034>
- Saravanan A, Kumar PS, Vo D-VN, Yaashikaa PR, Karishma S, Jeevanantham S, Gayathri B, Bharathi VD (2021) Photocatalysis for removal of environmental pollutants and fuel production: a review. *Environ Chem Lett* 19(1):441–463. <https://doi.org/10.1007/s10311-020-01077-8>
- Sharma S, Dutta V, Raizada P, Hosseini-Bandegharai A, Singh P, Nguyen V-H (2021) Tailoring cadmium sulfide-based photocatalytic nanomaterials for water decontamination: a review. *Environ Chem Lett* 19(1):271–306. <https://doi.org/10.1007/s10311-020-01066-x>
- Soni V, Raizada P, Kumar A, Hasija V, Singal S, Singh P, Hosseini-Bandegharai A, Thakur VK, Nguyen V-H (2021) Indium sulfide-based photocatalysts for hydrogen production and water cleaning: a review. *Chem. Lett, Environ*. <https://doi.org/10.1007/s10311-020-01148-w>
- Sudhaik A, Raizada P, Thakur S, Saini AK, Singh P, Hosseini-Bandegharai A, Lim J-H, Jeong DY, Nguyen V-H (2020a) Peroxymonosulphate-mediated metal-free pesticide photodegradation and bacterial disinfection using well-dispersed graphene oxide supported phosphorus-doped graphitic carbon nitride. *Appl Nanosci* 10(11):4115–4137. <https://doi.org/10.1007/s13204-020-01529-1>
- Sudhaik A, Raizada P, Thakur S, Saini RV, Saini AK, Singh P, Kumar Thakur V, Nguyen V-H, Khan AAP, Asiri AM (2020b) Synergistic photocatalytic mitigation of imidacloprid pesticide and antibacterial activity using carbon nanotube decorated phosphorus doped graphitic carbon nitride photocatalyst. *J Taiwan Inst Chem Eng* 113:142–154. <https://doi.org/10.1016/j.jtice.2020.08.003>
- Sushma C, Kumar SG (2017) C-N-S tridoping into TiO<sub>2</sub> matrix for photocatalytic applications: observations, speculations and contradictions in the codoping process. *Inorg Chem Front* 4(8):1250–1267. <https://doi.org/10.1039/C7QI00189D>
- Tada H, Mitsui T, Kiyonaga T, Akita T, Tanaka K (2006) All-solid-state Z-scheme in CdS–Au–TiO<sub>2</sub> three-component nanojunction system. *Nature Mater* 5(10):782–786. <https://doi.org/10.1038/nmat1734>
- Tao J, Yu X, Liu Q, Liu G, Tang H (2021) Internal electric field induced S-scheme heterojunction MoS<sub>2</sub>/CoAl LDH for enhanced photocatalytic hydrogen evolution. *J Colloid Interface Sci* 585:470–479. <https://doi.org/10.1016/j.jcis.2020.10.028>
- Tong R, Ng KW, Wang X, Wang S, Wang X, Pan H (2020) Two-dimensional materials as novel co-catalysts for efficient solar-driven hydrogen production. *J Mater Chem A* 8(44):23202–23230. <https://doi.org/10.1039/D0TA08045D>
- Wang D, Xu Y, Sun F, Zhang Q, Wang P, Wang X (2016) Enhanced photocatalytic activity of TiO<sub>2</sub> under sunlight by MoS<sub>2</sub> nanodots modification. *Appl Surf Sci* 377:221–227. <https://doi.org/10.1016/j.apsusc.2016.03.146>
- Wang J, Wang G, Cheng B, Yu J, Fan J (2021) Sulfur-doped g-C<sub>3</sub>N<sub>4</sub>/TiO<sub>2</sub> S-scheme heterojunction photocatalyst for Congo Red photodegradation. *Chinese J Catal* 42(1):56–68. [https://doi.org/10.1016/S1872-2067\(20\)63634-8](https://doi.org/10.1016/S1872-2067(20)63634-8)
- Wang J, Zhang Q, Deng F, Luo X, Dionysiou DD (2020a) Rapid toxicity elimination of organic pollutants by the photocatalysis of environment-friendly and magnetically recoverable step-scheme SnFe<sub>2</sub>O<sub>4</sub>/ZnFe<sub>2</sub>O<sub>4</sub> nano-heterojunctions. *Chem Eng J* 379:122264. <https://doi.org/10.1016/j.cej.2019.122264>
- Wang R, Shen J, Zhang W, Liu Q, Zhang M, Zulfiqar T, H. (2020b) Build-in electric field induced step-scheme TiO<sub>2</sub>/W<sub>18</sub>O<sub>49</sub> heterojunction for enhanced photocatalytic activity under visible-light irradiation. *Ceramics Int* 46(1):23–30. <https://doi.org/10.1016/j.ceramint.2019.08.226>
- Wang W, Li G, Xia D, An T, Zhao H, Wong PK (2017) Photocatalytic nanomaterials for solar-driven bacterial inactivation: recent progress and challenges. *Environ Sci Nano* 4(4):782–799. <https://doi.org/10.1039/C7EN00063D>
- Wang Y, Suzuki H, Xie J, Tomita O, Martin DJ, Higashi M, Kong D, Abe R, Tang J (2018) Mimicking natural photosynthesis: solar to renewable H<sub>2</sub> fuel synthesis by Z-scheme water splitting systems. *Chem Rev* 118(10):5201–5241. <https://doi.org/10.1021/acs.chemrev.7b00286>
- Wang Y, Wang K, Wang J, Wu X, Zhang G (2020c) Sb<sub>2</sub>WO<sub>6</sub>/BiOBr 2D nanocomposite S-scheme photocatalyst for NO removal. *J Mater Sci Technol* 56:236–243. <https://doi.org/10.1016/j.jmst.2020.03.039>
- Wu Y-T, Yu Y-H, Nguyen V-H, Lu K-T, Wu JC-S, Chang L-M, Kuo C-W (2013) Enhanced xylene removal by photocatalytic oxidation using fiber-illuminated honeycomb reactor at ppb level. *J Hazard Mater* 262:717–725. <https://doi.org/10.1016/j.jhazmat.2013.09.037>
- Xia P, Cao S, Zhu B, Liu M, Shi M, Yu J, Zhang Y (2020a) Designing a 0D/2D s-scheme heterojunction over polymeric carbon nitride for visible-light photocatalytic inactivation of bacteria. *Angew Chem Int Ed* 59(13):5218–5225. <https://doi.org/10.1002/anie.201916012>
- Xia X, Song M, Wang H, Zhang X, Sui N, Zhang Q, Colvin VL, Yu WW (2019) Latest progress in constructing solid-state Z scheme photocatalysts for water splitting. *Nanoscale* 11(23):11071–11082. <https://doi.org/10.1039/C9NR03218E>
- Xia Y, Zhang L, Hu B, Yu J, Al-Ghamdi AA, Wageh S (2020b) Design of highly-active photocatalytic materials for solar fuel production. *Chem Eng J*. <https://doi.org/10.1016/j.cej.2020.127732>
- Xiao N, Li S, Li X, Ge L, Gao Y, Li N (2020) The roles and mechanism of cocatalysts in photocatalytic water splitting to produce hydrogen. *Chinese J Catal* 41(4):642–671. [https://doi.org/10.1016/S1872-2067\(19\)63469-8](https://doi.org/10.1016/S1872-2067(19)63469-8)
- Xie Q, He W, Liu S, Li C, Zhang J, Wong PK (2020) Bifunctional S-scheme g-C<sub>3</sub>N<sub>4</sub>/Bi/BiVO<sub>4</sub> hybrid photocatalysts toward artificial carbon cycling. *Chinese J Catal* 41(1):140–153. [https://doi.org/10.1016/S1872-2067\(19\)63481-9](https://doi.org/10.1016/S1872-2067(19)63481-9)
- Xu C, Ravi Anusuyadevi P, Aymonier C, Luque R, Marre S (2019a) Nanostructured materials for photocatalysis. *Chem Soc Rev* 48(14):3868–3902. <https://doi.org/10.1039/C9CS00102F>
- Xu F, Meng K, Cheng B, Wang S, Xu J, Yu J (2020a) Unique S-scheme heterojunctions in self-assembled TiO<sub>2</sub>/CsPbBr<sub>3</sub> hybrids for CO<sub>2</sub> photoreduction. *Nat Commun* 11(1):4613. <https://doi.org/10.1038/s41467-020-18350-7>
- Xu Q, Ma D, Yang S, Tian Z, Cheng B, Fan J (2019b) Novel g-C<sub>3</sub>N<sub>4</sub>/g-C<sub>3</sub>N<sub>4</sub> S-scheme isotype heterojunction for improved photocatalytic hydrogen generation. *Appl Surf Sci* 495:143555. <https://doi.org/10.1016/j.apsusc.2019.143555>



- Xu Q, Zhang L, Cheng B, Fan J, Yu J (2020b) S-Scheme Heterojunction Photocatalyst. *Chem* 6(7):1543–1559. <https://doi.org/10.1016/j.chempr.2020.06.010>
- Xu Q, Zhang L, Yu J, Wageh S, Al-Ghamdi AA, Jaroniec M (2018) Direct Z-scheme photocatalysts: principles, synthesis, and applications. *Mater Today* 21(10):1042–1063. <https://doi.org/10.1016/j.mattod.2018.04.008>
- Yang X, Wang D (2018) Photocatalysis: from fundamental principles to materials and applications. *ACS Appl Energy Mater* 1(12):6657–6693. <https://doi.org/10.1021/acsaem.8b01345>
- Ye L, Liu J, Gong C, Tian L, Peng T, Zan L (2012) Two Different roles of metallic Ag on Ag/AgX/BiOX (X = Cl, Br) visible light photocatalysts: surface plasmon resonance and Z-scheme bridge. *ACS Catal* 2(8):1677–1683. <https://doi.org/10.1021/cs300213m>
- Yu J, Wang S, Low J, Xiao W (2013) Enhanced photocatalytic performance of direct Z-scheme g-C<sub>3</sub>N<sub>4</sub>-TiO<sub>2</sub> photocatalysts for the decomposition of formaldehyde in air. *Phys Chem Chem Phys* 15(39):16883–16890. <https://doi.org/10.1039/C3CP53131G>
- Yu JC-C, Nguyen V-H, Lasek J, Wu JCS (2017) Titania nanosheet photocatalysts with dominantly exposed (001) reactive facets for photocatalytic NO<sub>x</sub> abatement. *Appl Catal B* 219:391–400. <https://doi.org/10.1016/j.apcatb.2017.07.077>
- Yuan Y-J, Li Z, Wu S, Chen D, Yang L-X, Cao D, Tu W-G, Yu Z-T, Zou Z-G (2018) Role of two-dimensional nanointerfaces in enhancing the photocatalytic performance of 2D–2D MoS<sub>2</sub>/CdS photocatalysts for H<sub>2</sub> production. *Chem Eng J* 350:335–343. <https://doi.org/10.1016/j.cej.2018.05.172>
- Zhang B, Shi H, Yan Y, Liu C, Hu X, Liu E, Fan J (2021) A novel S-scheme 1D/2D Bi<sub>2</sub>S<sub>3</sub>/g-C<sub>3</sub>N<sub>4</sub> heterojunctions with enhanced H<sub>2</sub> evolution activity. *Colloids Surf A Physicochem Eng Asp* 608:125598. <https://doi.org/10.1016/j.colsurfa.2020.125598>
- Zhang L, Ran J, Qiao S-Z, Jaroniec M (2019) Characterization of semiconductor photocatalysts. *Chem Soc Rev* 48(20):5184–5206. <https://doi.org/10.1039/C9CS00172G>
- Zhang S, Xu D, Chen X, Zhang S, An C (2020a) Construction of ultrathin 2D/2D g-C<sub>3</sub>N<sub>4</sub>/In<sub>2</sub>Se<sub>3</sub> heterojunctions with high-speed charge transfer nanochannels for promoting photocatalytic hydrogen production. *Appl Surf Sci* 528:146858. <https://doi.org/10.1016/j.apsusc.2020.146858>
- Zhang W, Mohamed AR, Ong W-J (2020b) Z-Scheme photocatalytic systems for carbon dioxide reduction: where are we now? *Angew Chem Int Ed* 59(51):22894–22915. <https://doi.org/10.1002/anie.201914925>
- Zhang Y, Xu J, Mei J, Sarina S, Wu Z, Liao T, Yan C, Sun Z (2020c) Strongly interfacial-coupled 2D–2D TiO<sub>2</sub>/g-C<sub>3</sub>N<sub>4</sub> heterostructure for enhanced visible-light induced synthesis and conversion. *J Hazard Mater* 394:122529. <https://doi.org/10.1016/j.jhazmat.2020.122529>
- Zheng Z, Zu X, Zhang Y, Zhou W (2020) Rational design of type-II nano-heterojunctions for nanoscale optoelectronics. *Mater Today Phys* 15:100262. <https://doi.org/10.1016/j.mtphys.2020.100262>
- Zhong S, Xi Y, Chen Q, Chen J, Bai S (2020) Bridge engineering in photocatalysis and photoelectrocatalysis. *Nanoscale* 12(10):5764–5791. <https://doi.org/10.1039/C9NR10511E>
- Zhou P, Yu J, Jaroniec M (2014) All-solid-state Z-scheme photocatalytic systems. *Adv Mater* 26(29):4920–4935. <https://doi.org/10.1002/adma.201400288>
- Zhu D, Zhou Q (2019) Action and mechanism of semiconductor photocatalysis on degradation of organic pollutants in water treatment: a review. *Environ Nanotechnol Monit Manag* 12:100255. <https://doi.org/10.1016/j.enmm.2019.100255>
- Zhu S, Wang D (2017) Photocatalysis: basic principles, diverse forms of implementations and emerging scientific opportunities. *Adv Energy Mater* 7(23):1700841. <https://doi.org/10.1002/aenm.201700841>
- Zhu Z, Zhou F, Zhan S (2020) Enhanced antifouling property of fluorocarbon resin coating (PEVE) by the modification of g-C<sub>3</sub>N<sub>4</sub>/Ag<sub>2</sub>WO<sub>4</sub> composite step-scheme photocatalyst. *Appl Surf Sci* 506:144934. <https://doi.org/10.1016/j.apsusc.2019.144934>
- Zou J, Deng W, Jiang J, Arramel He X, Li N, Fang J, Hsu JP (2020) Built-in electric field-assisted step-scheme heterojunction of carbon nitride-copper oxide for highly selective electrochemical detection of p-nonylphenol. *Electrochim Acta* 354:136658. <https://doi.org/10.1016/j.electacta.2020.136658>